



FAST Survey of HI and OH Absorption toward Extragalactic Radio Sources

Yogesh Chandola¹ , D. J. Saikia² , Yin-Zhe Ma³ , Zheng Zheng^{4,5}, Chao-Wei Tsai^{4,6,7} , Di Li^{8,4} , Denis Tramonte⁹ , and Hengxing Pan¹⁰

¹ Purple Mountain Observatory, Chinese Academy of Sciences, 10, Yuan Hua Road, Qixia District, Nanjing 210023, People's Republic of China; yogesh.chandola@pmo.ac.cn

² Inter-University Centre for Astronomy and Astrophysics (IUCAA), Pune University Campus, Ganeshkhind, Pune 411007, India

³ Department of Physics, Stellenbosch University, Matieland 7602, South Africa

⁴ National Astronomical Observatories, Chinese Academy of Sciences, 20A Datun Road, Beijing 100101, People's Republic of China

⁵ Key Laboratory of Radio Astronomy and Technology, Chinese Academy of Sciences, Beijing 100101, People's Republic of China

⁶ Institute for Frontiers in Astronomy and Astrophysics, Beijing Normal University, Beijing 102206, People's Republic of China

⁷ School of Astronomy and Space Science, University of Chinese Academy of Sciences, Beijing 100049, People's Republic of China

⁸ Department of Astronomy, Tsinghua University, Beijing 100084, People's Republic of China

⁹ Department of Physics, Xi'an Jiaotong-Liverpool University, 111 Ren'ai Road, Suzhou Dushu Lake Science and Education Innovation District, Suzhou Industrial Park, Suzhou 215123, People's Republic of China

¹⁰ Astrophysics, University of Oxford, Denys Wilkinson Building, Keble Road, Oxford, OX1 3RH, UK

Received 2024 April 8; revised 2024 June 17; accepted 2024 June 27; published 2024 September 17

Abstract

Neutral atomic hydrogen and molecular gas in the host galaxies of radio active galactic nuclei can be traced using HI 21 cm and OH-1667 MHz absorption lines to understand the fueling and feedback processes. We present the results of an HI and OH absorption survey with the Five-hundred-meter Aperture Spherical radio Telescope toward 40 radio sources of low–intermediate radio luminosity ($\sim 10^{23}$ – 10^{26} W Hz⁻¹ at 1.4 GHz), red mid-infrared color (W2[4.6 μ m]–W3[12 μ m] > 2.5 mag), and redshift up to 0.35. From 13 sources with good data at HI observing frequencies, we report the detection of HI absorption toward eight sources, five of which are new detections, including four in the redshift range 0.25–0.35. Our detection rates are consistent with our previous results, with the dependence on the star formation history of the host galaxies reflected in the mid-infrared Wide-field Infrared Survey Explorer W2–W3 colors and the compactness of the radio sources. We find no significant dependence of the detection rates on radio luminosity or redshift. We also find that the HI column densities are anticorrelated with the low-frequency spectral indices ($\alpha_{150\text{ MHz}}^{1.4\text{ GHz}}$, $S_\nu \propto \nu^{-\alpha}$). We do not have any detections from 23 sources with good data at OH observing frequencies. However, by stacking the spectra, we estimate the 3σ upper limit of the OH column density to be $2.27 \times 10^{14} T_{\text{ex}}/10\text{ K} \times 1/f_c\text{ cm}^{-2}$. By stacking the OH spectra for seven associated HI absorbers, we get a 3σ upper limit of $3.47 \times 10^{14} T_{\text{ex}}/10\text{ K} \times 1/f_c\text{ cm}^{-2}$ on the OH column density and 1.78×10^{-7} on the [OH]/[HI] ratio.

Unified Astronomy Thesaurus concepts: AGN host galaxies (2017); Active galaxies (17); Radio continuum emission (1340); HI line emission (690); Radio active galactic nuclei (2134); Radio spectroscopy (1359)

1. Introduction

Radio active galactic nuclei (AGNs) are classified based on their optical emission-line strengths into high-excitation-mode and low-excitation-mode AGNs, namely high-excitation radio galaxies (HERGs) and low-excitation radio galaxies (LERGs; Hine & Longair 1979; Laing et al. 1994; Buttiglione et al. 2010; Best & Heckman 2012; Heckman & Best 2014). This classification is mainly attributed to the differences in accretion modes of the two types of AGNs (Heckman & Best 2014). HERGs are efficiently-accreting-mode radio AGNs with high Eddington ratios, while LERGs are inefficiently-accreting-mode radio AGNs with low Eddington ratios (Heckman & Best 2014). Fueling and feedback processes are also believed to be different in the two types of AGNs. LERGs are said to be fueled due to the cooling of hot halo gas through Bondi accretion (Bondi 1952; Allen et al. 2006; Hardcastle et al. 2007) or chaotic accretion (Gaspari et al. 2013; Tremblay et al. 2018), while HERGs are said to be fueled due to mergers

(Hopkins et al. 2006; Ellison et al. 2013) or secular processes (Kormendy & Ho 2013). Also, the feedback in LERGs is largely in the form of radio jets, while it is mainly due to radiation in HERGs (Heckman & Best 2014). AGN feedback can have significant positive or negative effects on star formation in the host galaxy (Harrison 2017; Mulcahey et al. 2022; Davies et al. 2024; Harrison & Ramos Almeida 2024). Mechanical feedback due to jet–interstellar medium (ISM) interaction can cause gaseous outflows (Morganti et al. 1998, 2003, 2013). However, it also depends upon how the jet couples with the ISM. Simulations suggest that the coupling efficiency depends on the radio power and jet orientation (Mukherjee et al. 2018a, 2018b). Low-power highly inclined jets toward the disk can get trapped in the ISM and have a longer interaction time than higher-power and less inclined jets (Mukherjee et al. 2018a, 2018b). Jet–cloud interactions may also significantly affect the evolution of the radio source itself (see Saikia 2022 for a review). While sources with strong radio power could evolve into large radio sources, some weak radio sources can be trapped in the dense ISM and could die early, before they evolve into larger radio sources (Kunert-Bajraszewska et al. 2010; An & Baan 2012). At the lower redshifts ($z < 0.1$) and low radio luminosities, it is the LERGs that dominate the radio source population (Heckman & Best 2014).

Cold gas plays an important role in star formation and, hence, in the evolution of galaxies. Hydrogen, being the most abundant element in the Universe, largely forms the gas reservoir for star formation activity and fueling AGNs. Studying atomic hydrogen (HI) in the host galaxies of radio AGNs can provide answers to questions related to fueling the central engine and its feedback to the host galaxy and nearby environment. Hence, it is important to study the kinematics and distributions of HI gas in the host galaxies of radio AGNs and their surroundings to understand their co-evolution. In the literature, 21 cm HI absorption toward radio AGNs has been used to probe the gas properties in the host galaxies and circumnuclear regions of radio AGNs (e.g., Vermeulen et al. 2003; Gupta et al. 2006; Chandola et al. 2011, 2013, 2020; Geréb et al. 2015; Maccagni et al. 2017; Grasha et al. 2019; Murthy et al. 2021, 2022; Morganti et al. 2023). Unlike HI emission, HI absorption is detected from the gas clouds intersecting lines of sight to the background radio source. Hence, the detection also depends upon geometrical as well as physical factors. However, due to its dependence on the brightness of the background source, HI absorption is advantageous for detecting neutral hydrogen at higher redshifts and smaller scales (see Morganti & Oosterloo 2018 for a review). The compact radio AGNs (projected linear sizes of less than a few kiloparsecs) have higher HI absorption detection rates compared to extended large radio sources (projected linear sizes > 20 kpc), mainly because these sources have larger covering factors and trace the denser regions of HI gas (Pihlström et al. 2003; Vermeulen et al. 2003; Gupta et al. 2006; Chandola et al. 2011; Curran et al. 2013). Also, the host galaxies of compact radio AGNs have been suggested to be gas-rich as compared to the host galaxies of larger radio sources at nearby redshifts (Emonts et al. 2010). In our earlier work, we found that in the low–intermediate-radio-luminosity samples, LERGs have lower HI absorption detection rates compared to HERGs, largely because of their gas- and dust-poor host galaxies (Chandola et al. 2020). HI absorption detection rates largely depend upon the mid-infrared Wide-field Infrared Survey Explorer (WISE) W2–W3 colors of the host galaxies and the compactness of the radio sources at relatively nearby redshifts (Chandola & Saikia 2017; Chandola et al. 2020). At higher redshifts, the detection rates have been affected by selection effects, such as by samples of higher UV and radio luminosities, in earlier observations. This has resulted in largely low detection rates at higher redshifts, either due to high ionization or high spin temperature or both (Curran et al. 2008, 2019; Aditya et al. 2016; Aditya & Kanekar 2018a; Curran 2024).

1.1. Low-luminosity Radio Sources, HI Absorption, and FAST

Due to the sensitivity limitations of radio telescopes, the early HI absorption experiments were largely done toward bright radio sources selected from flux-density-limited samples. This has biased the HI absorption samples toward the higher-radio-luminosity sources ($> 10^{26}$ W Hz $^{-1}$ at 1.4 GHz), especially at higher redshifts (e.g., Aditya et al. 2016; Aditya & Kanekar 2018a, 2018b). Since the low-radio-luminosity radio sources follow a different evolutionary trajectory/phase compared to higher-luminosity sources, it is important to study the HI environment and its evolution for these sources. Over the past decade and longer, efforts toward studying HI absorption toward low–intermediate-radio-luminosity ($\sim 10^{23}$ – 10^{26} W Hz $^{-1}$

at 1.4 GHz) sources have increased, though they have been limited to nearby radio sources (Maccagni et al. 2017; Chandola et al. 2020). Maccagni et al. (2017) studied HI absorption toward approximately 250 sources at low redshifts ($z < 0.25$) and low–intermediate radio luminosities. The 19-beam receiver of the Five-hundred-meter Aperture Spherical radio Telescope (FAST; Nan et al. 2011) allows probing of the HI gas in lower-radio-luminosity sources to slightly larger redshifts of up to 0.35, due to its wide bandwidth and better sensitivity. Thus, it helps in understanding the redshift evolution of the HI gas environment of low-radio-luminosity sources and also in making comparisons with higher-luminosity objects in a limited redshift range to understand the effects of radio luminosity on HI properties. FAST, with its unprecedented sensitivity and broad bandwidth, may also help to detect broad blueshifted profiles reflecting outflowing gas due to jet–cloud interactions or radiation or starburst (Su et al. 2023). In this paper, we present the results from a survey of HI absorption toward radio AGNs of low radio luminosities up to a redshift of 0.35. In the redshift range 0.25–0.35, this is the lowest-radio-luminosity survey of all surveys thus far. In this paper, we report the HI absorption detection toward the four lowest-radio-luminosity sources to date in this redshift range.

1.2. OH Absorption and FAST

Tracing the cold molecular gas that is directly associated with the star formation activity in host galaxies is also important for understanding the feedback effects of AGNs. The diffuse molecular gas in the ISM can be also traced with the hydroxyl (OH) molecule (Li et al. 2018). OH can be detected in four hyperfine transitions, mostly at 1667 MHz. Other lines at 1665 MHz, 1612 MHz, and 1720 MHz are weak or absent (McBride et al. 2013). To date, only two radio AGNs—B3 1504+377 and PKS 1413+135—have been detected with associated OH absorption lines (Kanekar & Chengalur 2002). Using FAST for the pilot OH absorption study toward three radio AGNs detected in HI absorption, Zheng et al. (2020) obtained an upper limit on the OH column density ($\sim 1.57 \times 10^{14} T_{\text{ex}}/10 \text{ K} \times 1/f_{\text{c}} \text{ cm}^{-2}$) and its ratio with the HI column density ($< 5.45 \times 10^{-8}$). The cosmic evolution of several physical constants—such as the electron–proton mass ratio $\mu = m_p/m_e$, the fine-structure constant $\alpha = e^2/\hbar$, and the proton g -factor g_p —can also be constrained using the cospatial HI and OH absorption lines (Kanekar et al. 2005). Large surveys to detect the rare coincidence of HI 21 cm and OH 18 cm absorption lines can be conducted with the large bandwidth of the FAST 19-beam receiver. Many sources within the redshift range of 0.1499–0.35 can be searched for simultaneous HI absorption as well as OH absorption using the FAST 19-beam receiver.

In this paper, we present the results of an HI and OH absorption survey using FAST toward 40 low–intermediate-luminosity ($\sim 10^{23}$ – 10^{26} W Hz $^{-1}$ at 1.4 GHz) radio sources from Best & Heckman (2012) with red mid-infrared color (W2–W3 > 2.5 mag) up to the redshift of 0.35. The paper is arranged as follows. In Section 2, we describe our sample selection, observations, and data reduction. In Section 3, we present our results, and in Section 3.1, we list individual HI absorption cases. We discuss our results in Section 4 and, finally, we summarize our results in Section 5. Throughout the paper, we have used the concordance cosmology $\Omega_{\text{m}} = 0.3$, $\Omega_{\Lambda} = 0.7$, and $H_0 = 70 \text{ km s}^{-1} \text{ Mpc}^{-1}$.

2. Sample, Observation, and Data Reduction

We selected a sample of 76 radio sources from Best & Heckman (2012), with their peak flux densities $>40 \text{ mJy beam}^{-1}$ at 1.4 GHz in the Faint Images of the Radio Sky at Twenty-Centimetres (FIRST; Becker et al. 1995) survey, their mid-infrared ALLWISE (Cutri et al. 2021) color $W2[4.6 \mu\text{m}] - W3[12 \mu\text{m}] > 2.5 \text{ mag}$, and redshift < 0.35 . The redshift cutoff of below 0.35 was given so that the observing HI frequency lies above 1050 MHz, the low-frequency limit of the FAST 19-beam feed receiver. We also selected sources with unresolved radio structures in the FIRST survey based on the ratios of the NRAO-VLA Sky Survey (NVSS; Condon et al. 1998) flux density to the FIRST flux density (< 1.2) and the FIRST integrated-to-peak radio flux densities (< 1.2). We further removed sources with earlier studies in HI absorption, except those with redshift > 0.1499 (corresponding to an observing frequency of 1450 MHz for the OH 1667 MHz spectral line), to study the OH absorption. This left us with 55 sources. A further nine sources were removed that had previous observations with FAST, which gave us 46 sources. Of these 46 sources, 40 were observed with FAST. Of these 40, 22 have been classified as LERGs and 18 as HERGs by Best & Heckman (2012). We have listed these 40 sources in Table 1. For 39 sources, we also have low-frequency spectral indices ($\alpha_{150 \text{ MHz}}^{1.4 \text{ GHz}}, S_\nu \propto \nu^{-\alpha}$) from de Gasperin et al. (2018), estimated using flux densities from the TIFR-GMRT Sky Survey (TGSS; Intema et al. 2017) and NVSS. The 1.4 GHz radio luminosities of these sources are in the range $\sim 10^{23.4} \text{ W Hz}^{-1}$ to $10^{26.1} \text{ W Hz}^{-1}$, with a median value $\sim 10^{25} \text{ W Hz}^{-1}$ (see Figure 1). In Figure 1, we have also shown the relative positions of the earlier HI absorption studies toward low-intermediate-radio-luminosity sources from Maccagni et al. (2017), Murthy et al. (2021), and Yu et al. (2023) in the luminosity–redshift plot for comparison. Most of the sources in our sample in the redshift range 0.25–0.35 have radio luminosities lower than those from Murthy et al. (2021).

We observed these 40 radio sources with FAST in ON–OFF mode from 2021 September to 2022 June (project ID: PT2021_0034). The observational details are provided in Table 2. Of these 40 sources, for one source, SDSS J141327.22+550529.2, observations failed, due to a problem in the control system. Of the remaining 39 sources, 30 could also be observed for OH absorption simultaneously. We used an ON/OFF source period of 180 s in each ON–OFF cycle, except for J133242.53+134253.8, where we used 205 s. Following Zheng et al. (2020), the OFF source positions for beam M01 were selected $\sim 11'8$ toward the east in R.A., such that another beam, M14, directs toward the ON source position. The data were sampled with a sampling time of ~ 1 s. For calibration, we injected high noise (~ 10 K) for ~ 1 s after every 10 s.

The data were reduced using a Python-based spectral line data reduction pipeline developed by us. The pipeline first combines the data from all the raw FITS files and then separates them for each ON–OFF cycle. The pipeline then converts the power into the antenna temperature (T_a) for each cycle, using the equation

$$T_a = \frac{P_{\text{caloff}} T_{\text{cal}}}{P_{\text{calon}} - P_{\text{caloff}}}, \quad (1)$$

where P_{calon} and P_{caloff} are the power measured when the noise injection is ON and OFF, respectively. T_{cal} is the temperature of the noise injected. After conversion to T_a , time and

frequency stamps affected by radio frequency interference (RFI) are masked and average values of the ON source antenna temperature ($T_{a,\text{ON}}$) and OFF source antenna temperature ($T_{a,\text{OFF}}$) are obtained for each cycle. For each cycle, we obtain the brightness temperature T_b by subtracting $T_{a,\text{OFF}}$ from $T_{a,\text{ON}}$. The brightness temperature T_b spectra are obtained for different cycles and averaged together. A high-degree polynomial and the sine wave function are fitted outside the expected spectral line portion in the spectrum. These functions are subtracted from this spectrum for the XX and YY polarizations separately, to subtract the continuum and remove the ripples. The spectrum is then averaged for XX and YY polarizations and converted to millijansky using the gains for different beams from Jiang et al. (2020) when the zenith angle is less than $26^\circ.4$. For the cases where the zenith angle is greater than $26^\circ.4$, the gains are estimated using Equation (3) of Zhang et al. (2019). The frequencies are then converted to velocities using the optical definitions and corrected for Doppler shift due to the Earth’s motion around the Sun using the `astropy` library. Finally, the spectra from beams M01 and M14 were averaged together to get the final spectrum when both beams had good data. The typical spectral resolution of the final spectrum is $\sim 2 \text{ km s}^{-1}$ (7.63 kHz), which we further Hanning-smoothed to the velocity resolutions given in Tables 3 and 4.

3. Results

Of the total 40 sources, we find only 13 sources for which we could either detect HI in absorption or set upper limits due to the effects of RFI. The rest of the sources were badly affected by RFI from satellites and for one source observations failed, due to a problem in the control system. Of these 13 sources, HI absorption was detected in eight sources, resulting in a detection rate¹¹ of $61.5_{-21.3}^{+30.4}\%$. In Figures 2 and 3, we present the HI profiles toward these 13 sources. While three sources—J135223.46–015648.4, J145844.79+372021.5, and J213333.31–071249.2—have previously been reported in the literature, we find five new cases of HI absorption, namely J090410.36+024744.8, J095058.69+375758.8, J122228.47+171437.3, J133242.53+134253.8, and J233515.92–011216.8. The detections toward J122228.47+171437.3 and J133242.53+134253.8 are of 3σ significance, while the other detections have $>5\sigma$ significance. The optical depth from the absorbed flux density was determined using the equation (Morganti & Oosterloo 2018)

$$\tau = -\ln\left(1 + \frac{\Delta S}{f_c S_c}\right), \quad (2)$$

where ΔS , f_c , and S_c are the continuum-subtracted line flux density, covering factor, and continuum flux density at the spectral line frequency, respectively. We assume a covering factor of 1 for our calculations. The median optical depth $\tau_{\text{rms}}(\text{HI})$ is 0.0103 for all 13 sources. We further fitted the Gaussian function to these profiles to obtain the FWHM, shift in velocities with respect to the optical systemic velocities (V_{shift}), and peak optical depth (τ_{peak}). We list all the parameters from the profiles in Table 3. We estimated the

¹¹ We estimated the 1σ error on detection rates using the Gehrels (1986) small number statistics for the Poisson distribution.

Table 1
Radio Sources Observed with FAST

(1) Source Name	(2) Redshift	(3) LERG/HERG	(4) S _{NVSS} (mJy)	(5) S _{FIRST} (mJy)	(6) S _{FIRST} (peak) (mJy beam ⁻¹)	(7) α _{150 MHz} ^{1.4 GHz}	(8) log P _{1.4 GHz} (W Hz ⁻¹)	(9) W2–W3 (mag)
SDSS J022246.94–093848.7	0.30617 ± 0.00004	LERG	56.7	57.38	55.32	0.19	25.1	4.05
SDSS J081437.98+172208.3	0.17919 ± 0.00004	LERG	37.8	53.92	51.86	< –0.15 ^a	24.4	2.60
SDSS J081755.21+312827.4	0.12376 ± 0.00002	HERG	69.2	61.48	53.3	0.63	24.4	3.81
SDSS J083216.03+183212.1	0.15411 ± 0.00002	HERG	896.0	874.24	852.06	–0.41	25.7	2.77
SDSS J083548.14+151717.0	0.16838 ± 0.00003	LERG	44.8	48.66	46.31	...	24.5	2.57
SDSS J090410.36+024744.8	0.27691 ± 0.00003	LERG	45.2	48.26	46.94	< –0.47 ^a	24.9	3.68
SDSS J092527.55+072641.6	0.12896 ± 0.00002	LERG	104.4	103.07	97.06	0.56	24.6	3.61
SDSS J092924.92+193421.0	0.30330 ± 0.00007	LERG	112.3	111.27	106.05	–0.55	25.3	3.90
SDSS J093242.81–003948.8	0.23534 ± 0.00001	HERG	44.2	46.16	45.32	< –0.51 ^a	24.7	3.31
SDSS J094310.82+295203.6	0.29941 ± 0.00006	LERG	54.4	57.68	55.66	0.12	25.1	>2.67
SDSS J095058.69+375758.8	0.04053 ± 0.00001	HERG	66.6	68.26	67.51	< –0.54 ^a	23.4	3.01
SDSS J102453.63+233234.0	0.16462 ± 0.00002	LERG	108.9	125.13	121.33	–0.26	24.8	2.77
SDSS J110701.20+182548.8	0.17856 ± 0.00002	HERG	162.7	159.93	142.03	0.77	25.1	2.79
SDSS J114538.51+442021.9	0.29974 ± 0.00004	LERG	362.3	327.31	309.35	0.46	26.0	2.78
SDSS J115712.38–032107.7	0.08202 ± 0.00002	LERG	50.7	52.71	50.61	0.29	23.9	2.84
SDSS J121755.30–033723.3	0.18229 ± 0.00003	HERG	213.6	208.26	176.68	0.63	25.3	2.57
SDSS J122113.25–024859.5	0.11300 ± 0.00002	LERG	100.3	105.56	98.16	–0.29	24.5	2.57
SDSS J122228.47+171437.3	0.31894 ± 0.00006	HERG	49.6	47.4	47.17	0.14	25.1	2.59
SDSS J124419.96+405136.8	0.24934 ± 0.00002	HERG	361.2	367.63	345.89	0.59	25.8	2.68
SDSS J124707.32+490017.9	0.20691 ± 0.00002	LERG	1204.8	1212.7	1037.73	0.40	26.1	2.54
SDSS J132522.00+035848.9	0.25479 ± 0.00005	LERG	113.5	113.29	111.12	0.34	25.3	2.56
SDSS J132859.25+173842.3	0.18035 ± 0.00003	HERG	158.6	158.78	152.77	0.30	25.1	2.92
SDSS J133242.53+134253.8	0.28287 ± 0.00002	HERG	57.1	52.67	47.74	0.81	25.1	2.98
SDSS J135223.46–015648.4	0.16694 ± 0.00001	HERG	529.6	552.19	479.26	0.72	25.6	2.53
SDSS J141327.22+550529.2	0.28156 ± 0.00006	LERG	125.9	128.48	125.77	–0.039	25.4	2.96
SDSS J143806.13+190954.9	0.18854 ± 0.00002	HERG	45.4	44.52	43.16	0.76	24.6	2.84
SDSS J144920.71+422101.2	0.17862 ± 0.00006	HERG	155.7	165.64	159.08	–0.38	25.0	3.20
SDSS J145844.79+372021.5	0.33331 ± 0.00008	LERG	214.8	269.97	266.39	–0.31	25.7	2.91
SDSS J152142.58+181438.2	0.15043 ± 0.00006	HERG	92.1	93.27	90.9	0.74	24.7	3.86
SDSS J153016.25+375831.2	0.15171 ± 0.00002	HERG	104.9	99.82	98.53	< –0.62 ^a	24.7	3.27
SDSS J153229.40+015133.7	0.12326 ± 0.00001	LERG	79.0	81.92	79.53	0.42	24.5	3.37
SDSS J153836.11+552541.4	0.19117 ± 0.00005	HERG	209.2	209.84	184.22	0.72	25.3	2.60
SDSS J154345.80+110935.9	0.10231 ± 0.00002	LERG	48.1	48.22	47.73	0.21	24.1	2.70
SDSS J155903.43+230828.7	0.19318 ± 0.00004	LERG	43.6	44.95	43.67	0.29	24.6	2.53
SDSS J155927.67+533054.4	0.17921 ± 0.00001	HERG	182.7	182.35	170.43	0.97	25.2	2.86
SDSS J162033.43+173955.5	0.16361 ± 0.00002	LERG	107.1	111.44	104.23	< –0.26 ^a	24.8	3.27
SDSS J213333.31–071249.2	0.08654 ± 0.00001	HERG	189.8	200.5	194.78	0.57	24.5	4.26
SDSS J230551.18–104052.2	0.18970 ± 0.00002	LERG	69.9	70.34	66.42	0.21	24.8	3.36
SDSS J233515.92–011216.8	0.26988 ± 0.00003	LERG	45.7	45.85	42.07	0.72	25.0	3.85
SDSS J235400.91–003449.5	0.32593 ± 0.00008	LERG	66.6	67.72	66.43	< –0.31 ^a	25.2	2.54

Notes. Column (1): source name. Column (2): heliocentric redshifts from SDSS (Ahumada et al. 2020) DR16. Column (3): LERG or HERG classification, based on Best & Heckman (2012). Column (4): NVSS flux density in units of millijansky. Column (5): FIRST integrated flux density in units of millijansky. Column (6): peak FIRST flux density in units of millijansky per beam. Column (7): spectral index (α_{150 MHz}^{1.4 GHz}) from de Gasperin et al. (2018) estimated using flux density values from TGSS (Intema et al. 2017) and NVSS—the spectral index is defined as S_ν ∝ ν^{–α}. Column (8): logarithm of luminosity at 1.4 GHz in units of W Hz^{–1} estimated using NVSS flux densities. Column (9): ALLWISE W2[4.6 μm]–W3[12 μm] color in Vega magnitude.

^a Source is not detected in TGSS. The spectral index upper limit has been estimated using the 3σ upper limit on the noise value in the TGSS image.

column densities using the equation (Wolfe & Burbidge 1975)

$$N(\text{HI}) = 1.823 \times 10^{18} T_s \int \tau dv \text{ cm}^{-2}, \quad (3)$$

where we assume a spin temperature $T_s = 100$ K and $\int \tau dv$ is the integrated optical depth, which for a Gaussian profile is given by $1.064 \times \text{FWHM} \times \tau_{\text{peak}}$. We estimated the errors on the integrated optical depth using $\tau_{\text{rms}} \times \delta v \times \sqrt{\frac{\text{FWZI}}{\delta v}}$. We assume the full width zero intensity (FWZI) to be $2.547 \times \text{FWHM}$ for a Gaussian profile. The median HI column density for HI detections has been estimated to be $9.46 \times 10^{20} \text{ cm}^{-2}$. The 3σ

upper limits on HI integrated optical depths were obtained by assuming a Gaussian profile of $\text{FWHM} = 100 \text{ km s}^{-1}$ and using $3 \times \tau_{\text{rms}} \times \delta v \times \sqrt{\frac{\text{FWZI}}{\delta v}}$. The median $N(\text{HI})$ 3σ upper limit for HI nondetections has been estimated to be $2.72 \times 10^{20} \text{ cm}^{-2}$, which is similar to the median upper limits of $2.6 \times 10^{20} \text{ cm}^{-2}$ achieved with our earlier observations (Chandola et al. 2020) using the Giant Metrewave Radio Telescope (GMRT) or $3.5 \times 10^{20} \text{ cm}^{-2}$ by Maccagni et al. (2017).

In addition to HI absorption, we have 23 spectra unaffected by RFI at their OH observing frequencies (shown in Figure 4). We obtained a median τ_{rms} (OH) of 0.0064. We did not detect

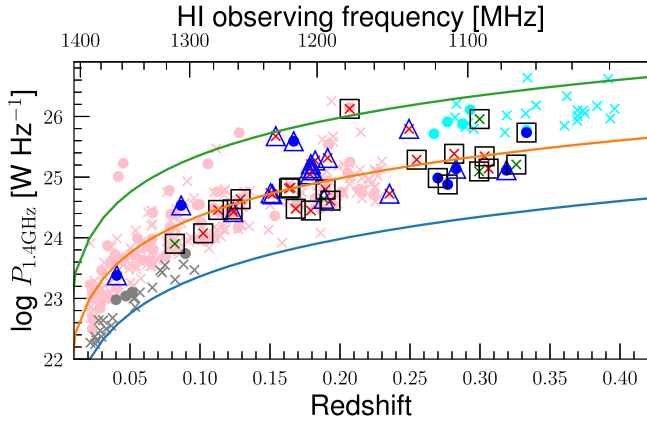


Figure 1. Radio luminosity at 1.4 GHz vs. redshift. The H I observing frequencies are shown on the upper X-axis. The sources observed with FAST, shown with black squares and blue triangles, represent LERGs and HERGs, respectively. The sources with H I absorption detections are marked with the blue filled circles, while nondetections and RFI-affected or failed observations are marked with the green and red crosses, respectively. For comparison, we have also shown the sources with previous H I absorption studies of low–intermediate radio luminosity below a redshift of 0.4 from Maccagni et al. (2017), Murthy et al. (2021), and Yu et al. (2023), with the pink, cyan, and gray colored circles (detections) and crosses (nondetections), respectively. The solid blue, orange, and green lines mark the sources with flux densities of 10 mJy, 100 mJy, and 1000 mJy at 1.4 GHz, respectively.

OH absorption in any of these sources, although it is possible in the source J133242.53+134253.3 at a blueshifted velocity of $\sim 400 \text{ km s}^{-1}$, which needs to be probed from deeper observations. We estimated the upper limits on the OH column densities using the equation (Liszt & Lucas 1996)

$$N(\text{OH}) = 2.24 \times 10^{14} T_{\text{ex}} \int \tau dv \text{ cm}^{-2}, \quad (4)$$

where we assume the excitation temperature ($T_{\text{ex}} = 10 \text{ K}$) and obtain the integrated optical depth using FWZI, assuming a line FWHM = 100 km s^{-1} . For the sources detected with H I absorption, we use the FWZI of the full H I absorption lines. For the sources with multiple Gaussian components, we determined the FWZI of the full profile using $(V_{\text{high}} + \text{FWZI}_{\text{high}}/2) - (V_{\text{low}} - \text{FWZI}_{\text{low}}/2)$, where “high” and “low” are the Gaussian components at the highest and lowest velocities. For all OH nondetections, we achieved a median 3σ upper limit of $1.74 \times 10^{15} \text{ cm}^{-2}$. This median upper limit on the OH column density is similar to the median OH column density value of $1.92 \times 10^{15} \text{ cm}^{-2}$ for four intervening OH absorbers reported in the literature (Kanekar & Chengalur 2002; Kanekar & Briggs 2003; Kanekar et al. 2012; Gupta et al. 2018). We have listed the upper limits for all 23 sources in Table 4.

Of these 23 sources, we have H I absorption data for five sources: J090410.36+024744.8, J133242.53+134253.8, J135223.46–015648.4, J143806.13+190954.9, and J233515.92–011216.8. These include the detections J090410.36+024744.8, J133242.53+134253.8, J135223.46–015648.4, and J233515.92–011216.8. We achieved a median 3σ upper limit of $1.62 \times 10^{15} \text{ cm}^{-2}$ on the OH column density of these four sources. For the source J153836.11+552541.4, although, due to the presence of RFI, we could not confirm the H I absorption we had earlier detected with the GMRT (Chandola et al. 2020), we have RFI-free OH spectra in this paper. Similarly, for the sources J083548.14+151717.0 and J124707.32+490017.9, Maccagni

et al. (2017) had reported H I absorption, which we could not detect due to RFI, but we have OH spectra. We further stacked the OH absorption spectra of these seven associated H I absorber detections and all OH nondetections separately (see Figure 5), by normalizing using the variance, i.e., $1/\tau_{\text{rms}}^2$, in these profiles. For the stacked OH spectrum of seven H I absorbers, we obtained $\tau_{\text{rms}}(\text{OH})$ of 0.00122, which corresponds to a 3σ upper limit on the OH column density of $3.47 \times 10^{14} \text{ cm}^{-2}$. Using the mean H I column density, $19.5 \times 10^{20} \text{ cm}^{-2}$, for seven H I absorbers, we estimated an $[\text{OH}]/[\text{H I}]$ upper limit of 1.78×10^{-7} . For the stacked OH spectra of all OH nondetections, we obtained $\tau_{\text{rms}}(\text{OH})$ of 0.0008, which corresponds to a 3σ upper limit on the OH column density of $2.27 \times 10^{14} \text{ cm}^{-2}$.

3.1. Individual Sources with H I Absorption

3.1.1. New Sources with H I Absorption Detections

J090410.36+024744.8. We detected H I absorption toward this source at a redshift of 0.27691. This source has been classified as a LERG by Best & Heckman (2012). The peak flux density in FIRST is $46.94 \text{ mJy beam}^{-1}$ and the integrated flux density is 48.26 mJy . This source is unresolved in FIRST. It has a radio luminosity of $\sim 10^{25} \text{ W Hz}^{-1}$ at 1.4 GHz. The radio continuum spectrum shows inversion ($\alpha_{150 \text{ MHz}}^{1.4 \text{ GHz}} < 0$) at lower frequencies, as it is not detected in the TGSS image. The H I absorption profile has four Gaussian components, three blueshifted and one redshifted, all within $\pm 100 \text{ km s}^{-1}$ of the optical redshift. The multiple-component profile suggests the complex motion of the gas. The H I column density has been estimated to be $(101.92 \pm 1.78) \times 10^{20} \text{ cm}^{-2}$.

J095058.69+375758.8. J095058.69+375758.8 is a Seyfert 1 galaxy at a redshift of 0.04053 and classified as a HERG by Best & Heckman (2012). The optical Sloan Digital Sky Survey (SDSS) image shows an edge-on disk-like morphology. The radio power of the source is $\sim 10^{23.4} \text{ W Hz}^{-1}$, with a peak flux density of $67.5 \text{ mJy beam}^{-1}$ in FIRST. The continuum radio spectrum shows inversion at lower frequencies, with no detection in the TGSS image. We detect H I emission as well as absorption toward this source. The H I absorption component is a narrow (FWHM $\sim 29.9 \text{ km s}^{-1}$) and deep ($\tau_{\text{peak}} \sim 0.9$) profile redshifted by $\sim 54.6 \text{ km s}^{-1}$ relative to the optical systemic velocity. The H I column density for the H I absorbing component has been estimated to be $(51.90 \pm 0.46) \times 10^{20} \text{ cm}^{-2}$.

J122228.47+171437.3. This radio source is a HERG at a redshift of 0.31894, corresponding to an H I observing frequency of 1076.9298 MHz. It has a flat continuum radio spectrum ($\alpha_{150 \text{ MHz}}^{1.4 \text{ GHz}} \sim 0.14$). This source shows an absorption feature in the profile at optical redshift, though at 3σ . We estimate an H I column density of $(2.57 \pm 0.67) \times 10^{20} \text{ cm}^{-2}$.

J133242.53+134253.8. This source is a HERG at a redshift of 0.28287, corresponding to an expected H I frequency of 1107.2094 MHz. It has a steep spectrum with a spectral index $\alpha_{150 \text{ MHz}}^{1.4 \text{ GHz}} \sim 0.82$. It could be a compact steep spectrum (CSS) or an extended radio source not resolved in the FIRST image. The SDSS optical image shows a possible tidal-tail-like merger feature. The H I spectrum shows a shallow absorption feature (optical depth ~ 0.013) of an FWHM of 114.2 km s^{-1} at around -294 km s^{-1} relative to the optical systemic velocity, though at 3σ significance. The H I column density has been estimated to be $(2.88 \pm 0.45) \times 10^{20} \text{ cm}^{-2}$.

J233515.92–011216.8. We detected H I absorption toward this radio source at a redshift of 0.26988. This source is

Table 2
Observational Details of the Search for Associated H I and OH Absorption

(1) Source Name	(2) H I Freq. (MHz)	(3) Beam(s) Used	(4) OH Freq. (MHz)	(5) Beam(s) Used	(6) Observation Date	(7) ON Source Time (s)
SDSS J022246.94–093848.7	1087.4586	RFI	1276.5253	RFI	2022 Jan 29	540
SDSS J081437.98+172208.3	1204.5606	RFI	1413.9867	M01, M14	2021 Oct 02	540
SDSS J081755.21+312827.4	1263.9761	RFI	1483.7323	OR	2021 Oct 05	360
SDSS J083216.03+183212.1	1230.7369	RFI	1444.7141	M01	2021 Oct 20	180
SDSS J083548.14+151717.0	1215.7053	RFI	1427.0691	M01, M14	2021 Oct 20	540
SDSS J090410.36+024744.8	1112.3773	M01, M14	1305.7764	M01	2021 Oct 23 and 2022 Jan 29	750
SDSS J092527.55+072641.6	1258.1542	RFI	1476.8982	OR	2021 Oct 22	360
SDSS J092924.92+193421.0	1089.8533	RFI	1279.3363	RFI	2021 Oct 18	180
SDSS J093242.81–003948.8	1149.8096	RFI	1349.7167	M01, M14	2022 Jan 30	720
SDSS J094310.82+295203.6	1093.1159	M01	1282.1662	RFI	2021 Oct 23	540
SDSS J095058.69+375758.8	1365.0791	M01	1602.4132	OR	2021 Nov 10	360
SDSS J102453.63+233234.0	1219.6302	RFI	1431.6764	M01, M14	2021 Oct 19	180
SDSS J110701.20+182548.8	1205.2044	RFI	1414.7426	M01, M14	2021 Nov 11	180
SDSS J114538.51+442021.9	1092.8384	M01	1282.8404	RFI	2021 Nov 18	180
SDSS J115712.38–032107.7	1312.7352	M01, M14	1540.9687	OR	2022 Jan 30	720
SDSS J121755.30–033723.3	1201.4022	RFI	1410.2792	M01, M14	2022 Feb 03	180
SDSS J122113.25–024859.5	1276.1956	RFI	1498.0764	OR	2021 Dec 02	180
SDSS J122228.47+171437.3	1076.9298	M01, M14	1264.1659	RFI	2022 Jan 30	720
SDSS J124419.96+405136.8	1136.9249	RFI	1334.5919	M01	2021 Nov 22	180
SDSS J124707.32+490017.9	1176.8945	RFI	1381.5106	M01	2021 Nov 23	180
SDSS J132522.00+035848.9	1131.9868	RFI	1328.7952	M01, M14	2021 Dec 19	180
SDSS J132859.25+173842.3	1203.3767	RFI	1412.5971	M01, M14	2021 Dec 17	180
SDSS J133242.53+134253.8	1107.2094	M01, M14	1299.7100	M01, M14	2022 Feb 02	615
SDSS J135223.46–015648.4	1217.2055	M01, M14	1428.8301	M01, M14	2021 Dec 12	180
SDSS J141327.22+550529.2	1108.3412	Failed	1301.0386	Failed	2021 Dec 20	180
SDSS J143806.13+190954.9	1195.0845	M01	1402.8632	M01	2022 Jan 31	900
SDSS J144920.71+422101.2	1205.1431	RFI	1414.6706	M01	2021 Dec 12	180
SDSS J145844.79+372021.5	1065.3230	M01	1250.5411	RFI	2022 Jan 03	180
SDSS J152142.58+181438.2	1234.6738	RFI	1449.3355	OR	2022 Jan 03	180
SDSS J153016.25+375831.2	1233.3016	RFI	1447.7247	M01	2021 Dec 20	180
SDSS J153229.40+015133.7	1264.5387	RFI	1484.3928	OR	2022 Jan 04	180
SDSS J153836.11+552541.4	1192.4459	RFI	1399.7658	M01	2022 Jan 07	180
SDSS J154345.80+110935.9	1288.5720	RFI	1512.6044	OR	2022 Jan 04	540
SDSS J155903.43+230828.7	1190.4371	RFI	1397.4078	M01, M14	2022 Feb 01	720
SDSS J155927.67+533054.4	1204.5401	RFI	1413.9627	M01	2022 Jan 05	180
SDSS J162033.43+173955.5	1220.6888	RFI	1432.9191	M01, M14	2022 Jan 05	180
SDSS J213333.31–071249.2	1307.2742	M14	1534.5583	OR	2021 Sep 20	180
SDSS J230551.18–104052.2	1193.9193	RFI	1401.4953	M01, M14	2021 Sep 27	540
SDSS J233515.92–011216.8	1118.5354	M01, M14	1313.0052	M01, M14	2022 Jun 01	720
SDSS J235400.91–003449.5	1071.2524	M01	1257.5015	RFI	2021 Sep 28	360

Notes. Column (1): source name. Column (2): H I 21 cm redshifted line frequency in megahertz. Column (3): beam(s) used in final H I spectra. Column (4): OH redshifted 1667.359 MHz line frequency in megahertz. Column (5): beam(s) used in final OH spectra. Column (6): date of observation. Column (7): ON target source time per beam in seconds. RFI: radio frequency interference; OR: out of frequency range; and failed: observation failed due to technical problems.

classified as a LERG by Best & Heckman (2012) and has a radio luminosity of $\sim 10^{24.8} \text{ W Hz}^{-1}$, with a steep low-frequency spectrum ($\alpha_{150 \text{ MHz}}^{1.4 \text{ GHz}} \sim 0.72$). The H I absorption is a narrow (FWHM $\sim 21.8 \text{ km s}^{-1}$) profile blueshifted by $\sim 99 \text{ km s}^{-1}$ relative to the optical systemic velocity. The H I column density has been estimated to be $(3.21 \pm 0.41) \times 10^{20} \text{ cm}^{-2}$.

3.1.2. H I Absorption Detection toward Radio Sources Previously Reported with H I Absorption

J135223.46–015648.4. We have reported H I absorption toward this source, a HERG at the redshift of 0.167, in our earlier paper (Chandola et al. 2020). This source has an H I absorption profile with two components: one broad and shallow component and another deep and narrow component. To make a comparison of the profiles obtained with the GMRT and

FAST, we plot the profiles together in Figure 2. This plot shows that the profiles are consistent from two different observations and FAST can detect shallow profiles of optical depth ~ 0.006 in a relatively short time.

This source has an extended resolved radio structure in the observations with the GMRT. Since the profiles from different spatial resolutions are similar, we conclude that the H I absorption is from the compact radio component. We used the peak flux density from GMRT observations to estimate the optical depth. We estimate an H I column density of $(9.49 \pm 0.46) \times 10^{20} \text{ cm}^{-2}$ from FAST observations, which is consistent within 1σ with our earlier GMRT results.

J145844.79+372021.5. This source is classified as a LERG by Best & Heckman (2012) at the redshift of 0.33331 ± 0.00008 . The low-frequency-radio-continuum spectrum of the source shows an inversion ($\alpha_{150 \text{ MHz}}^{1.4 \text{ GHz}} \sim -0.31$), indicating a possibility

Table 3
Results of the Search for Associated H I Absorption

(1) Source Name	(2) $S_c(\text{H I})$ (mJy bm^{-1})	(3) Vel. Res. (km s^{-1})	(4) $\Delta S_{\text{rms}}(\text{H I})$ (km s^{-1})	(5) $\tau_{\text{rms}}(\text{H I})$	(6) $\int \tau dv$ (km s^{-1})	(7) $N(\text{H I})$ (10^{20} cm^{-2})	(8) Gaussian No.	(9) V_{shift} (km s^{-1})	(10) FWHM (km s^{-1})	(11) τ_{peak}
SDSS J090410.36+024744.8	42.13	8.2	0.58	0.0139	55.91 ± 0.98	101.92 ± 1.78	1	-64.2	29.1	0.038
							2	-36.1	81.4	0.401
							3	-1.7	75.2	0.115
							4	41.2	51.0	0.199
SDSS J094310.82+295203.6	57.34	8.4	0.86	0.0150	<2.08	<3.79				
SDSS J095058.69+375758.8	66.56	6.8	0.76	0.0114	28.50 ± 0.25	51.95 ± 0.46	1	54.6	27.9	0.960
SDSS J114538.51+442021.9	346.68	8.3	1.31	0.0038	<0.52	<0.95				
SDSS J115712.38-032107.7	51.56	6.9	0.42	0.0081	<1.02	<1.86				
SDSS J122228.47+171437.3	48.93	11.4	0.43	0.0088	1.41 ± 0.34	2.57 ± 0.67	1	-1.2	50.9	0.026
SDSS J133242.53+134253.8	57.77	11.0	0.25	0.0043	1.58 ± 0.25	2.88 ± 0.45	1	-294.4	114.2	0.013
SDSS J135223.46-015648.4	361.2 ^a	7.5	1.17	0.0032	5.20 ± 0.22	9.49 ± 0.46	1	41.4	218.7	0.013
							2	154.7	34.7	0.059
SDSS J143806.13+190954.9	48.68	7.6	0.55	0.0113	<1.49	<2.72				
SDSS J145844.79+372021.5	183.0 ^b	2.1 ^c	2.22	0.0121	8.44 ± 0.04	15.39 ± 0.17	1	-33.1	11.4	0.696
SDSS J213333.31-071249.2	211.3 ^d	7.0	1.16	0.0055	5.17 ± 0.25	9.43 ± 0.45	1	58.3	48.6	0.100
SDSS J233515.92-011216.8	49.44	8.1	0.51	0.0103	1.76 ± 0.22	3.21 ± 0.41	1	-98.5	23.0	0.072
SDSS J235400.91-003449.5	61.14	8.5	0.78	0.0128	<1.78	<3.25				

Notes. Column (1): source name. Column (2): radio continuum flux density in millijansky per beam at the H I observing frequency, estimated using the FIRST peak flux density and spectral index from Table 1. Column (3): effective velocity resolution of the spectrum after smoothing. Column (4): rms noise in the absorption spectrum. Column (5): 1σ optical depth rms. Column (6): integrated optical depth or 3σ upper limit in kilometers per second. Column (7): column density or 3σ upper limit in units of 10^{20} cm^{-2} , with assumptions of a spin temperature of $T_s = 100 \text{ K}$ and a covering factor of $f_c = 1$. Column (8): Gaussian component number. Column (9): shift in the velocity of the Gaussian component relative to the optical systemic velocity in kilometers per second. Column (10): FWHM of the Gaussian component in kilometers per second. Column (11): peak optical depth of the Gaussian component.

^a We have used the peak flux density at the H I observing frequency from our earlier GMRT observations (Chandola et al. 2020) instead of the FIRST peak flux density.

^b Peak flux density value from Murthy et al. (2021).

^c No smoothing has been done for this profile.

^d Peak flux density value from Chandola et al. (2020).

Table 4
Results of the Search for Associated OH Absorption

(1) Source Name	(2) S_c (OH) (mJy bm^{-1})	(3) Vel. Res. (km s^{-1})	(4) ΔS_{rms} (OH) (km s^{-1})	(5) τ_{rms} (OH)	(6) $\int \tau dv$ (OH) (km s^{-1})	(7) $N(\text{OH})$ (10^{15} cm^{-2})	(8) $N(\text{OH})/N(\text{H I})$ 10^{-7}
SDSS J081437.98+172208.3	51.94	6.5	0.37	0.0070	<0.86	<1.93	...
SDSS J083216.03+183212.1	863.11	6.3	1.27	0.0015	<0.18	<0.40	...
SDSS J083548.14+151717.0 ^a	46.31	6.4	0.37	0.0081	<0.80 ^b	<1.79	<12.2
SDSS J090410.36+024744.8 ^a	45.43	7.0	0.63	0.0137	<1.70	<3.80	<3.7
SDSS J093242.81−003948.8	44.48	6.8	0.32	0.0072	<0.90	<2.03	...
SDSS J102453.63+233234.0	122.04	6.4	0.78	0.0064	<0.78	<1.74	...
SDSS J110701.20+182548.8	140.89	6.5	0.71	0.0050	<0.61	<1.38	...
SDSS J121755.30−033723.3	175.87	6.5	0.70	0.0040	<0.48	<1.08	...
SDSS J124419.96+405136.8	355.79	6.9	1.07	0.0030	<0.38	<0.84	...
SDSS J124707.32+490017.9 ^a	1043.26	6.6	1.59	0.0015	<0.28 ^b	<0.62	<73.9
SDSS J132522.00+035848.9	113.11	6.9	0.70	0.0062	<0.78	<1.74	...
SDSS J132859.25+173842.3	152.36	6.5	0.66	0.0043	<0.53	<1.18	...
SDSS J133242.53+134253.8 ^a	50.70	7.0	0.30	0.0059	<0.80	<1.80	<62.5
SDSS J135223.46−015648.4 ^a	321.88 ^c	6.4	0.83	0.0026	<0.41	<0.92	<9.7
SDSS J143806.13+190954.9	43.09	6.5	0.45	0.0104	<1.26	<2.83	...
SDSS J144920.71+422101.2	159.71	6.5	0.92	0.0057	<0.70	<1.57	...
SDSS J153016.25+375831.2	100.60	6.3	0.96	0.0096	<1.15	<2.58	...
SDSS J153836.11+552541.4 ^a	184.24	6.5	1.04	0.0057	<0.77 ^d	<1.73	<48.1
SDSS J155903.43+230828.7	43.69	6.5	0.29	0.0066	<0.80	<1.79	...
SDSS J155927.67+533054.4	168.80	6.5	1.20	0.0071	<0.86	<1.94	...
SDSS J162033.43+173955.5	104.86	6.4	0.83	0.0080	<0.96	<2.16	...
SDSS J230551.18−104052.2	66.41	6.5	0.54	0.0081	<0.99	<2.22	...
SDSS J233515.92−011216.8 ^a	44.06	7.0	0.47	0.0106	<0.64	<1.44	<44.9

Notes. Column (1): source name; Column (2): radio continuum flux density in millijansky per beam at the OH observing frequency, estimated using the FIRST peak flux density and spectral index from Table 1, except for J083548.14+151717.0, where we do not have the spectral index and use the FIRST peak flux density. Column (3): effective velocity resolution of the spectrum after smoothing. Column (4): rms noise in the absorption spectrum. Column (5): 1σ optical depth rms. Column (6): 3σ upper limit on integrated optical depth, assuming a line FWHM of 100 km s^{-1} , except for the sources with associated H I absorption, where we use the FWZI of the full H I absorption profiles. Column (7): 3σ upper limit on OH column densities in units of 10^{15} cm^{-2} , with assumptions of an excitation temperature of $T_{\text{ex}} = 10 \text{ K}$ and a covering factor of $f_c(\text{OH}) = 1$. Column (8): upper limits on $N(\text{OH})/N(\text{H I})$ in units of 10^{-7} for sources with associated H I absorption.

^a Sources detected with associated H I absorption.

^b Used $\int \tau dv$ (H I) and $\tau_{\text{peak}}(\text{H I})$ from Maccagni et al. (2017) to obtain the FWHM(H I) for a single Gaussian profile and converted to FWZI using $\text{FWZI} = 2.547 \times \text{FWHM}$.

^c Continuum flux density extrapolated to OH frequency using the flux density value for the H I frequency from Table 3 and the spectral index from Table 1.

^d Using Gaussian profile parameters from Chandola et al. (2020) to estimate FWZI.

of a peaked-spectrum (PS) source (O’Dea & Saikia 2021). However, this source was earlier classified as a flat-spectrum radio source, based on a spectral index of -0.46 between 1.4 and 4.85 GHz by Taylor et al. (1996). The very-long-baseline-interferometry-scale maps show a very compact radio structure of $\lesssim 10$ mas, corresponding to a projected linear size of $\lesssim 48$ pc (Helmboldt et al. 2007; Murthy et al. 2021). This source is classified as a blazar and could be a BL Lacertae (BL Lac) object (D’Abrusco et al. 2014).

This source has been reported with H I absorption earlier, by Aditya & Kanekar (2018a) and Murthy et al. (2021). The profile has a single deep (optical depth ~ 0.70) and narrow component (FWHM $\sim 11.4 \text{ km s}^{-1}$), reflecting absorption due to the H I disk. Although Aditya & Kanekar (2018a) and Murthy et al. (2021) found this profile to be blueshifted by ~ 60 and $\sim 40 \text{ km s}^{-1}$ relative to the optical redshift, the profile from FAST observations shows a smaller shift relative to the optical systemic velocity, with a blueshift of 33.1 km s^{-1} . It is to be noted that this difference could be due to the different redshift of 0.33343 (Schneider et al. 2005) used by Aditya & Kanekar (2018a). We also notice that the profile is deeper relative to the earlier observations by Aditya & Kanekar (2018a) and Murthy et al. (2021), resulting in a higher column density value of $\sim 15.4 \times 10^{20} \text{ cm}^{-2}$. This difference in the absorption profile

depth could result from the intrinsic variability of the source, with the compact radio component intersecting clouds of different depths during the different observation epochs.

J213333.31−071249.2. This source is a HERG at a redshift of 0.087 and has been reported with H I absorption in an earlier paper by us (Chandola et al. 2020). It has a steep low-frequency-radio-continuum spectrum ($\alpha_{1.4 \text{ GHz}/150 \text{ MHz}}^{1.4} \sim 0.57$). We compare the H I absorption profiles from GMRT and FAST. The two profiles are consistent, with a slight offset in velocity, but less than the spectral resolution. Although the GMRT profile appears slightly deeper, it is within the 10% error on gain calibration. We estimate the column density value to be $(9.43 \pm 0.45) \times 10^{20} \text{ cm}^{-2}$.

3.1.3. H I Absorption Nondetections

J094310.82+295203.6. This radio AGN is identified as a LERG by Best & Heckman (2012) at the SDSS optical redshift of 0.29941. The H I spectrum is partially affected due to RFI at 1090 MHz, requiring further checking. However, we categorize this source as a nondetection with an upper limit on the H I column density of $<3.79 \times 10^{20} \text{ cm}^{-2}$. It has a flat spectrum at low frequencies ($\alpha_{1.4 \text{ GHz}/150 \text{ MHz}}^{1.4} \sim 0.12$).

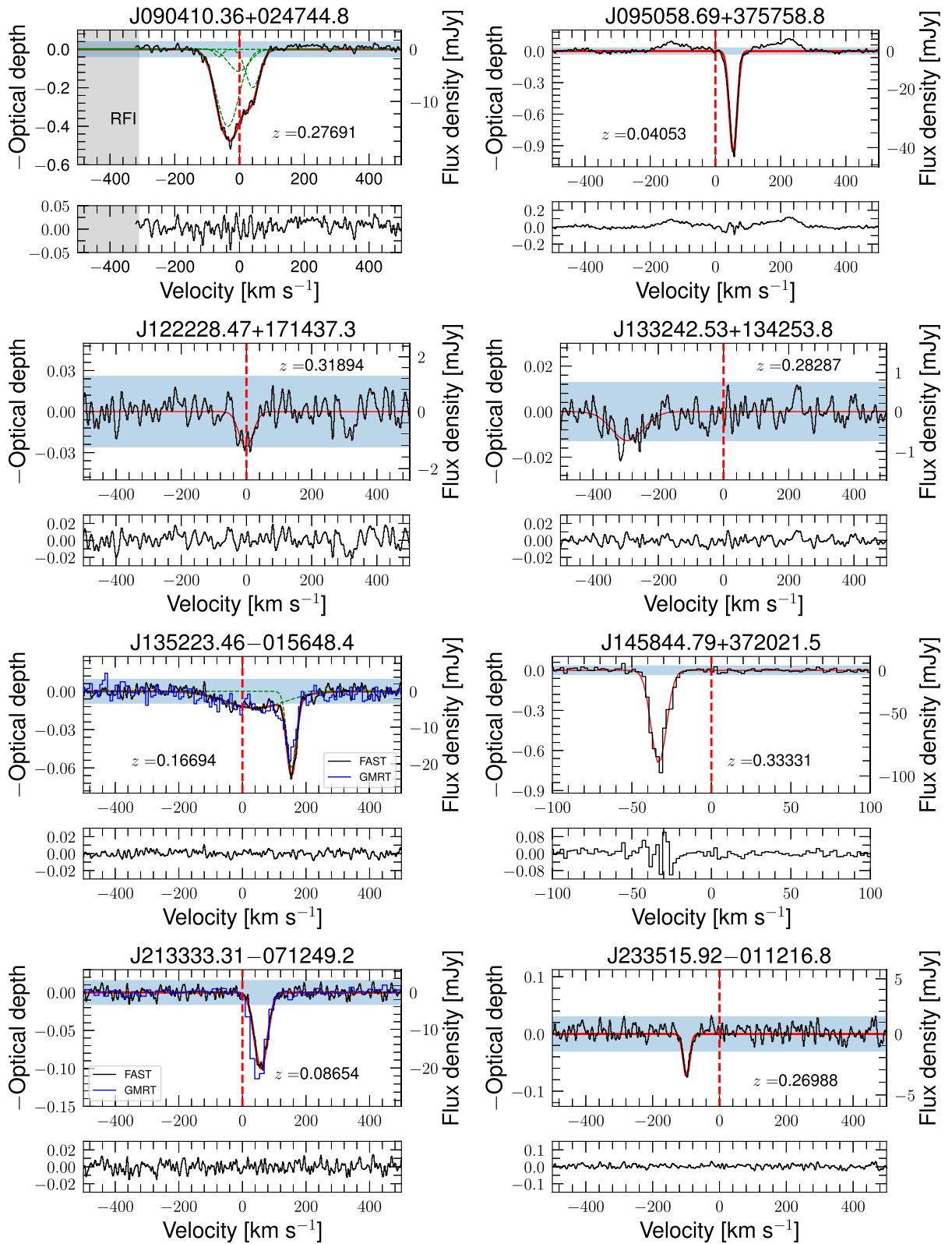


Figure 2. H I 21 cm spectra of the sources detected with absorption from FAST observations are shown in black. The X-axes represent the velocities with respect to the optical systemic velocity and the Y-axes on the left are optical depths, while continuum-subtracted flux densities are shown on the right. The red vertical dashed line at zero marks the optical redshift. The $3\sigma \tau_{\text{rms}}$ values are shown with the blue shading. The gray shading marks the velocities affected by RFI. The Gaussian profile components are shown with the green dashed lines, while the red solid line shows the combined Gaussian profile. The residuals from the fit are shown at the bottom panel of each plot.

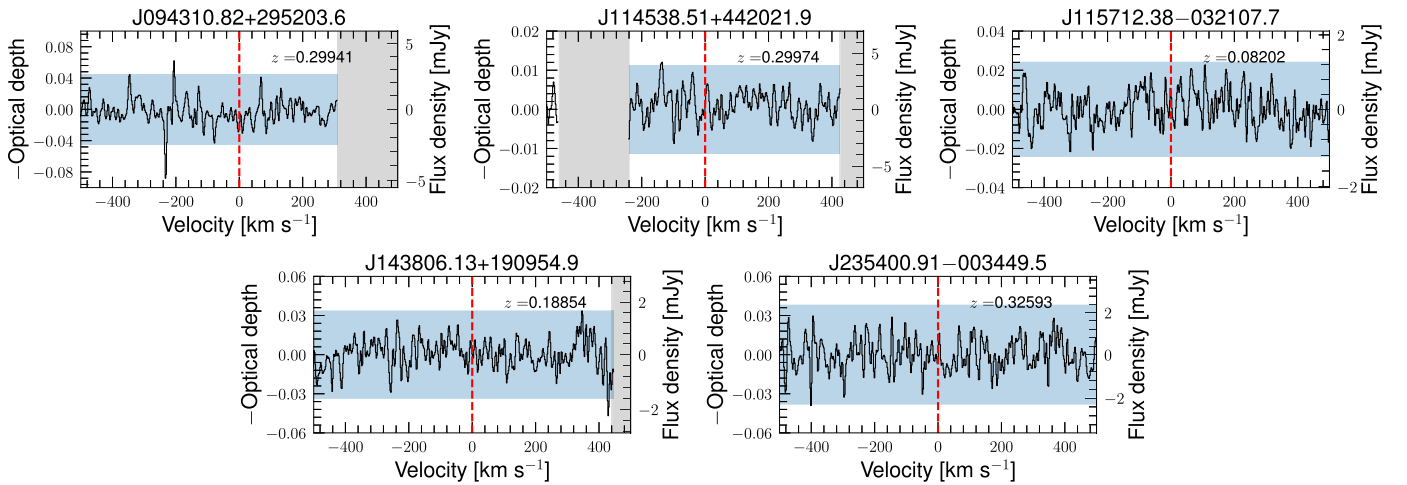


Figure 3. HI 21 cm spectra of the sources with no detection of absorption from FAST observations. The X-axes represent the velocities with respect to the optical systemic velocity and the Y-axes on the left are optical depths, while continuum-subtracted flux densities are shown on the right. The red vertical dashed line at zero marks the optical redshift. The $3\sigma \tau_{\text{rms}}$ values are shown with the blue shading. The gray shading marks the velocities affected by RFI.

J114538.51+442021.9. This source is a LERG at the redshift of 0.29974. A significant portion of the HI spectrum of this source is also affected by the RFI at 1090 MHz and hence needs further checking. However, from the velocities -200 to $+400$ km s^{-1} relative to the optical systemic velocity, we obtained a 3σ upper limit on $N(\text{HI})$ of $0.95 \times 10^{20} \text{ cm}^{-2}$. The low-frequency spectral index for this source is flat ($\alpha_{150 \text{ MHz}}^{1.4 \text{ GHz}} \sim 0.46$). This source is also identified among γ -ray-emitting blazars and it could be a BL Lac object (D’Abrusco et al. 2014; Peña-Herazo et al. 2021).

J115712.38-032107.7. This radio AGN is a LERG at the optical redshift of 0.08202, corresponding to an HI observing frequency of 1312.7352 MHz. This source also has a flat low-frequency radio continuum spectrum ($\alpha_{150 \text{ MHz}}^{1.4 \text{ GHz}} \sim 0.29$). We obtained a $3\sigma N(\text{HI})$ upper limit of $\sim 1.86 \times 10^{20} \text{ cm}^{-2}$.

J143806.13+190954.9. This source is a HERG at a redshift of 0.18854 (the corresponding HI frequency is 1195.0845 MHz). It has a steep-spectrum low-frequency spectral index ($\alpha_{150 \text{ MHz}}^{1.4 \text{ GHz}} \sim 0.76$), and hence it could be a CSS or extended radio source not resolved in the FIRST image. We did not detect HI absorption toward this source, and we provide an upper limit on the column density of $2.72 \times 10^{20} \text{ cm}^{-2}$.

J235400.91-003449.5. This is a LERG at a redshift of 0.32593, showing inversion at the low-frequency radio continuum spectrum with no detection in the TGSS. We obtained an upper limit of $3.25 \times 10^{20} \text{ cm}^{-2}$ on its HI column density.

4. Discussion

4.1. HI Absorption Detection Rates

In the literature, the dependence of HI absorption detection rates on many factors—such as the redshift, host galaxy star formation history, AGN type, radio source structure, and radio and UV luminosities—has been discussed. In this subsection, we explore the detection rates in our sample and discuss the effects of all these factors. In our earlier work, for the sources at relatively lower redshift ($z < 0.25$), we have found a strong dependence of HI absorption detection rates on mid-infrared WISE W2–W3 colors, reflecting the star formation history and dust-rich nature of the host galaxies (Chandola & Saikia 2017; Chandola et al. 2020). Those with redder W2–W3 > 2 values

were found to have higher detection rates ($\sim 50\%$) than those with lower values ($\sim 10\%$). We selected our current sample to be dust- and gas-rich, with $W2-W3 > 2.5$ occupying the region for luminous infrared galaxies or ultraluminous infrared galaxies or obscured AGNs (see Figure 6) in the WISE color-color diagram (Wright et al. 2010). For the sources with no significant RFI effects, we find an overall HI absorption detection rate of 8/13 ($61.5^{+30.4}_{-21.3}\%$), which is consistent with our earlier results.

We further consider the effect of low-frequency spectral indices ($\alpha_{150 \text{ MHz}}^{1.4 \text{ GHz}}$, $S_\nu \propto \nu^{-\alpha}$) on the column densities. The low-frequency spectral indices ($\alpha_{150 \text{ MHz}}^{1.4 \text{ GHz}}$) can be used as a proxy for radio structures in the absence of high-resolution radio maps. Those showing turnover or inversion below 1.4 GHz are likely to be PS sources. Sources with a steep spectrum ($\alpha_{150 \text{ MHz}}^{1.4 \text{ GHz}} > 0.5$) are believed to have extended structures, being CSS sources or larger in their projected linear sizes (O’Dea & Saikia 2021). Most of the sources with HI detection in our RFI-free sample (8/13) have either a flat ($\alpha_{150 \text{ MHz}}^{1.4 \text{ GHz}} \sim 0.0-0.5$) or inverted ($\alpha_{150 \text{ MHz}}^{1.4 \text{ GHz}} < 0$) radio spectrum, implying a compact nature. Most of the HERGs (4/6) in this sample are steep-spectrum sources, while LERGs (6/7) tend to have flat or inverted spectra. We find that there is an anticorrelation (Spearman’s R -value: -0.71 ; p -value: 0.046) between the HI column densities and $\alpha_{150 \text{ MHz}}^{1.4 \text{ GHz}}$, with those with an inverted spectrum having high HI column densities (see the top panel of Figure 7). This is consistent with the scenario of compact radio sources tracing higher-density regions (Pihlström et al. 2003) and possibly being confined due to high-density cold gas (An & Baan 2012).

Next, we consider the effect of central AGN accretion mode or strength. In our earlier paper, we found that the detection rates for LERGs and HERGs are similar at lower redshift ($z < 0.25$) if we have similar red mid-infrared colors of host galaxies and compact radio structures (Chandola et al. 2020). In this paper, we have expanded our work up to the redshift of 0.35. Given the small sample, in our current survey, the detection rate for HERGs, 5/6 ($83.3^{+56.4}_{-36.0}\%$), is similar within 1σ to the detection rate for LERGs, 3/7 ($42.9^{+41.7}_{-23.3}\%$), which is consistent with our earlier results—namely, if we consider LERGs and HERGs of similar redder WISE colors, the detection rates are similar. Our sample has UV luminosities

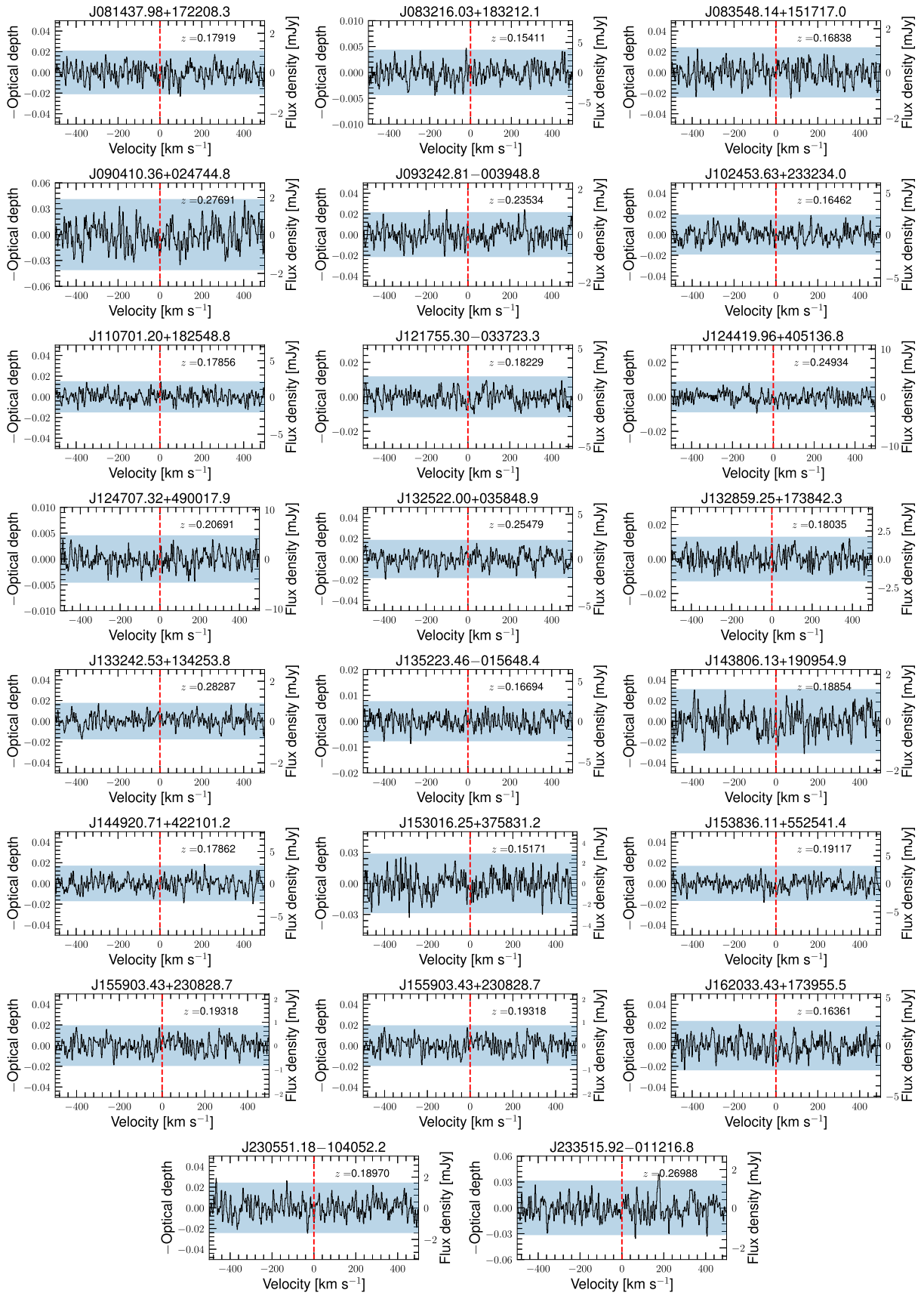


Figure 4. OH 1667 MHz spectra of 23 sources from FAST observations. The symbols mean the same as in Figure 3.

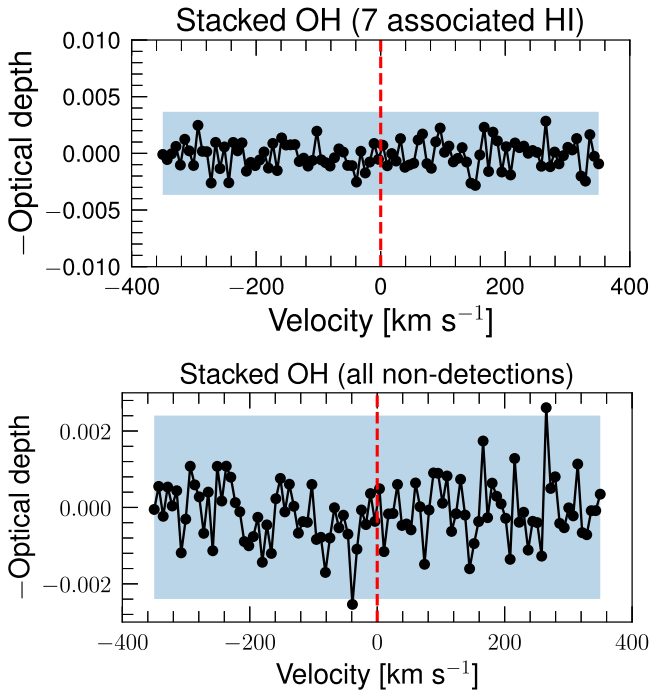


Figure 5. Top panel: stacked OH spectrum for seven known associated HI absorbers: 083548.14+151717.0, J090410.36+024744.8, J124707.32+490017.9, J135223.46-015648.4, J133242.53+134253.8, J153836.11+552541.4, and J233515.92-011216.8. We obtained an $\tau_{\text{rms}}(\text{OH})$ value of 0.00122 for this spectrum for a velocity resolution of 7 km s^{-1} , corresponding to the 3σ upper limit on $N(\text{OH})$ of $3.47 \times 10^{14} \text{ cm}^{-2}$. Bottom panel: stacked OH spectrum for all the nondetections shown in Figure 4. The $\tau_{\text{rms}}(\text{OH})$ value for this spectrum is 0.0008, which corresponds to the 3σ upper limit on $N(\text{OH})$ of $2.27 \times 10^{14} \text{ cm}^{-2}$.

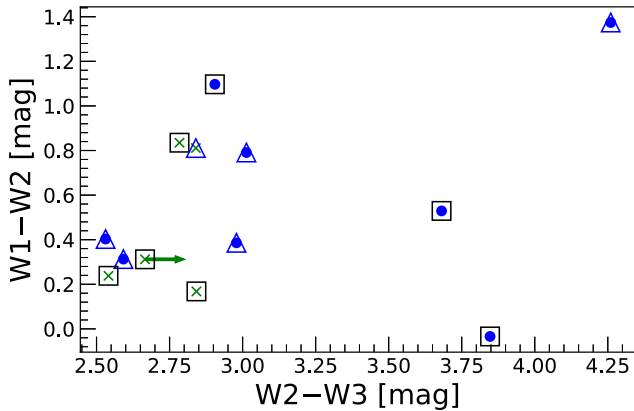


Figure 6. WISE W1–W2 vs. W2–W3 color–color plot for the sample of 13 sources with HI data not significantly affected by RFI. The symbols mean the same as in Figure 1. The arrow means the lower limit.

below $10^{23} \text{ W Hz}^{-1}$, the cutoff to ionize or excite the hydrogen atoms to higher levels (Curran 2024), and hence there is no effect of this on detection rates.

Radio luminosities and redshift may also affect the detection rates, with those with higher luminosity causing higher spin temperatures and the evolution of the gaseous environment with redshift. Of the 13 sources, eight sources lie in the redshift range $z > 0.25$ and have a detection rate of 5/8 ($62.5^{+42.3\%}_{-27.0\%}$), while those with $z < 0.25$ have a detection rate of 3/5 ($60^{+58.4\%}_{-32.7\%}$). This shows statistically no significant difference (see the middle panel of Figure 7). Of the eight sources at higher redshift, six are LERGs, and three detections are LERGs

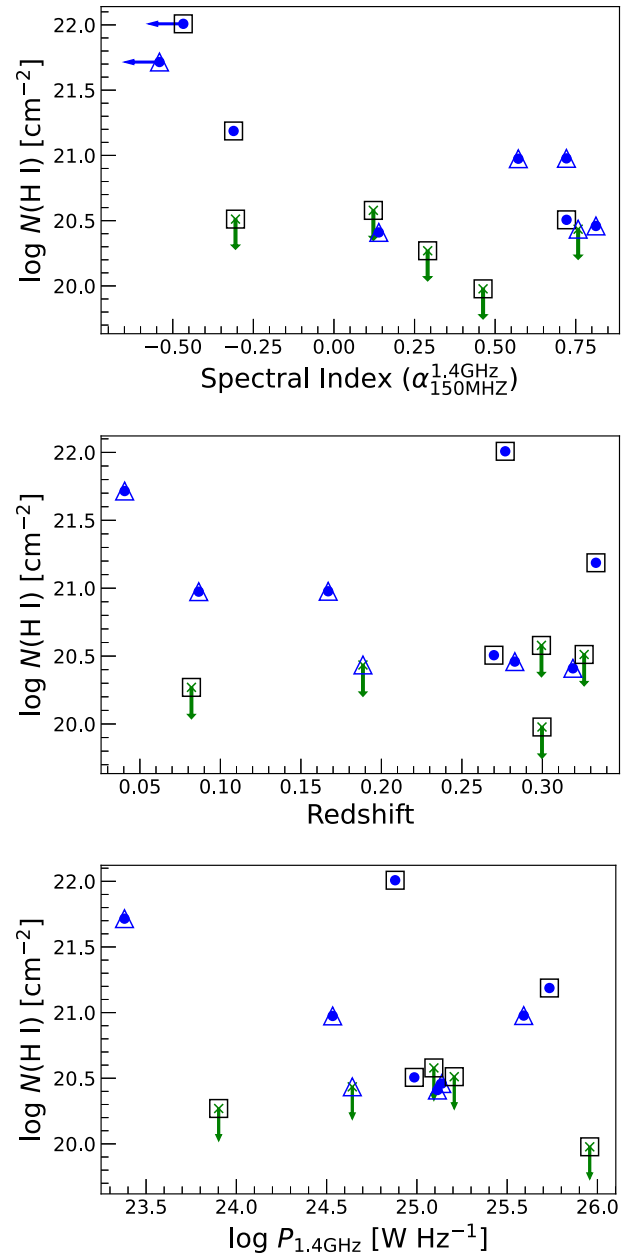


Figure 7. Top: $N(\text{H I})$ vs. low-frequency spectral index ($\alpha_{150 \text{ MHz}}^{1.4 \text{ GHz}}$). Middle: $N(\text{H I})$ vs. redshift. Bottom: $N(\text{H I})$ vs. log radio luminosity at 1.4 GHz. The arrows mean upper limits. The rest of the symbols mean the same as in Figure 1.

and the other two are HERGs. At the lower redshift, four of five sources are HERGs, and all three detections are HERGs. We also do not find any significant difference in the HI column densities with redshift for the sources with similar low–intermediate radio luminosities and WISE colors, though this needs to be checked from a larger sample.

Considering the full redshift range in our sample, we do not see any dependence of column density on radio luminosities. Our sample has sources with low–intermediate radio luminosities ($\lesssim 10^{26} \text{ W Hz}^{-1}$) only (see the bottom panel of Figure 7). Now, considering a limited redshift range of 0.25–0.4, there have been 67 sources (unaffected by RFI) studied in the literature, but with only 10 detections reported before our study (Vermeulen et al.

2003; Curran et al. 2006, 2011, 2017, 2019; Gupta et al. 2006; Yan et al. 2016; Ostorero et al. 2017; Aditya & Kanekar 2018a, 2018b; Grasha et al. 2019; Murthy et al. 2021; Mahony et al. 2022; Su et al. 2023). Murthy et al. (2021) studied a sample of intermediate-radio-luminosity ($\sim 10^{25.6}-10^{26.6}$ W Hz $^{-1}$ at 1.4 GHz) sources at $z \sim 0.25-0.4$ and found a detection rate of 5/26 ($\sim 19\%$). The detections in their sample are concentrated at lower redshifts, with a detection rate of 5/15 ($33.3^{+22.5}_{-14.4}\%$) in the redshift range of 0.25–0.35. As mentioned in Section 2, the sources at similar redshifts in our sample are of relatively low radio luminosities. While J145844.79+372021.5 is a common detection, four of our detections—J090410.36+024744.8, J122228.47+171437.3, J133242.53+134253.8, and J235515.92–011216.8—are among the lowest radio luminosity at the redshift range of 0.25–0.4. In this redshift range, earlier studies by Curran et al. (2006, 2011, 2017, 2019) have no detections from 15 sources. Similarly, Aditya & Kanekar (2018a, 2018b) have a very low detection rate, with only one detection toward J145844.79+372021.5, from 10 sources. However, Vermeulen et al. (2003) have a detection rate of 5/13 ($38.5^{+26.0}_{-16.6}\%$) toward radio sources of higher radio luminosities ($\gtrsim 10^{26}$ W Hz $^{-1}$). The different detection rates in these studies are possibly due to different sample selection criteria and the optical depth sensitivities of the observations. We find our detection rates (5/8, $62.5^{+42.3}_{-27.0}\%$) consistent with those of Vermeulen et al. (2003) within 1σ , implying no significant effect of radio luminosities on detection rates. However, our sample size and that of Vermeulen et al. (2003) are small in this limited redshift range and need to be probed from a larger sample.

4.2. HI Absorption Kinematics

HI absorption kinematics combined with radio AGN properties, such as morphology and radio power, have been used to interpret the nature of the absorbing medium in the host galaxies of radio AGNs in the literature. The interpretations of HI absorption profiles are largely based on profile parameters, such as the line width, its position relative to optical emission lines, the depth of the profile, and the number of components. The absorption profiles near the optical emission lines are interpreted as rotating disks (e.g., 3C 84—Morganti et al. 2023 and 4C 31.04—Murthy et al. 2024), which could be a circumnuclear torus or gas in the host galaxy. If the profile is redshifted with respect to optical lines, it could also be due to infalling gas (e.g., NGC 315—Morganti et al. 2009; B2352+495—Araya et al. 2010; and 4C 31.04—Struve & Conway 2012). Broad, shallow, and blueshifted absorption lines are usually interpreted as outflowing gas due to AGN or stellar feedback effects (e.g., IC 5063—Morganti et al. 1998; 3C 293—Morganti et al. 2003; and 4C 12.50—Morganti et al. 2013). It was found in earlier works that the compact sources show more incidences of blueshifted profiles suggesting outflowing gas (Chandola et al. 2013; Geréb et al. 2015; Maccagni et al. 2017). Also, the sources with higher radio power were found to have larger blueshifted and wider profiles (Chandola et al. 2011, 2020; Geréb et al. 2015; Chandola & Saikia 2017; Maccagni et al. 2017). Due to the low–intermediate radio luminosity, the sources in our sample do not show a large shift with respect to optical redshift, except for J133242.53+134253.8, which is blueshifted by ~ 300 km s $^{-1}$. Also, except for the sources J090410.36+024744.8, J133242.53+134253.8, and J135223.46–015648.4, all other absorption lines in our sample are narrow lines, with their FWHM < 100 km s $^{-1}$, indicating a settled HI gas in the galaxy disk. Possibly, most of

the radio sources in our sample are either too compact and/or less inclined toward the disk to have any significant jet–ISM interaction, as predicted by simulations (Mukherjee et al. 2018a, 2018b). For J090410.36+024744.8, multiple components of the Gaussian could be fitted, reflecting multiple absorbers in the ISM, although all components are within ± 100 km s $^{-1}$. In J135223.46–015648.4, the narrow, deep component redshifted by ~ 155 km s $^{-1}$ could be infalling gas, while the broader component could be a cloud closer to the central region, similar to the cases of NGC 315 and 4C 31.04 (Morganti et al. 2009; Struve & Conway 2012). Another possibility could be that the narrow profile is from the HI disk, but the orientation of the background radio source is such that the gas in front appears redshifted relative to the optical systemic velocity. In that scenario, the broader component may be due to jet–cloud interaction causing the outflow of cold gas, similar to 3C 293 (Morganti et al. 2003). In the case of J133242.53+134253.8, the broad, shallow, and blueshifted absorption profile could be due to jet–cloud interaction or unsettled gas from an earlier merger episode. It would require a detailed parsec-scale study to obtain further insights into detailed kinematics for these sources.

4.3. OH Absorption and Abundance

In Figure 8, we explore the abundance of OH compared to atomic HI gas. In an earlier paper, Zheng et al. (2020) found that [OH]/[HI] increased with redshift and, for the associated HI absorbers, the ratio has a lesser value compared to intervening absorbers in the literature. However, in our analysis, we find that sources in our sample with HI absorption have the upper limits on $N(\text{OH})$ being higher. The sources in our sample also have a higher average value of $N(\text{OH})/N(\text{HI})$ upper limits compared to Zheng et al. (2020) for a similar redshift range of $z < 0.35$. We have similar assumptions on the excitation temperature and covering factor, hence it is the higher upper limits on integrated optical depths that play a role. Since the spectral rms on optical depths are similar, it is because they are integrating within FWHM and we are integrating within a Gaussian FWZI (nearly $2.547 \times \text{FWHM}$) and they have a better spectral resolution of $\lesssim 2$ km s $^{-1}$ which results in a lower upper limit in their case. Also, the sources in our sample cover a wider range of HI column densities, with most of the sources (5/7) below 10^{21} cm $^{-2}$, while Zheng et al. (2020) have sources above 10^{21} cm $^{-2}$. Due to this, we have a higher upper limit on [OH]/[HI] for similar redshift.

Although, even after stacking, the upper limits on the OH column densities are lower for Zheng et al. (2020) due to the above reasons, the optical depth rms obtained by us are slightly better, suggesting these systems may have OH below our detection limit. The stacking results confirm the lower 3σ upper limits on $N(\text{OH}) \sim 3.47 \times 10^{14}$ cm $^{-2}$ for seven associated HI absorbers compared to the median value on $N(\text{OH}) \sim 1.92 \times 10^{15}$ cm $^{-2}$ for four intervening HI and OH absorption systems of similar HI column densities from the literature. It also confirms the lower 3σ upper limits on [OH]/[HI] $\sim 1.78 \times 10^{-7}$ in low–intermediate-redshift-associated HI systems compared to the value of 2.62×10^{-7} for the only higher redshift ($z \sim 0.673$) associated HI and OH absorber, B3 1504+377 (Kanekar & Chengalur 2002).

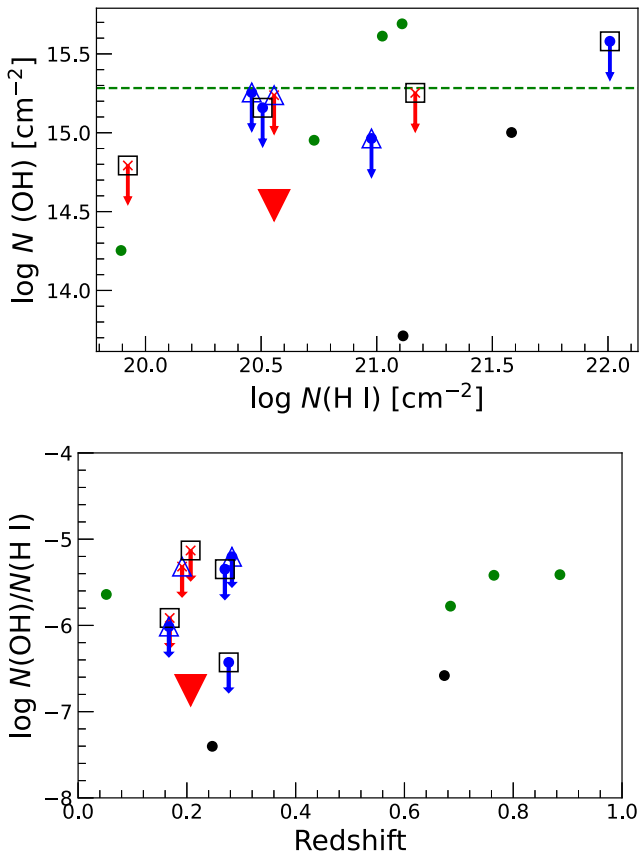


Figure 8. Top: $N(\text{OH})$ vs. $N(\text{H I})$. Bottom: $N(\text{OH})/N(\text{H I})$ vs. redshift. The green and black filled circles represent previous OH absorption detections from the literature toward intervening and associated H I absorption systems (Kanekar & Chengalur 2002; Kanekar & Briggs 2003; Kanekar et al. 2012; Gupta et al. 2018), respectively, which have been taken from the Zheng et al. (2020) compilation. In the top panel, the green dashed horizontal line marks the median value of $N(\text{OH})$ for four intervening OH absorbers in the literature. The red downward triangles represent the upper-limit values from stacking at their median $N(\text{H I})$ and redshift values in the top and bottom panels, respectively. The sources affected by RFI in our observations but reported with H I detections in the literature are shown with the red crosses. The arrows mean upper limits. The other symbols mean the same as in Figure 1. To estimate $N(\text{OH})$, we have used $T_{\text{ex}} = 10$ K and $f_{\text{c}}(\text{OH}) = 1$ for all sources in these plots. Similarly, for $N(\text{H I})$, we have used $T_{\text{s}} = 100$ K and $f_{\text{c}}(\text{H I}) = 1$ for all sources.

5. Conclusions

We have the following conclusions from our study, although our observations toward many sources (26 at H I frequencies and seven at OH frequencies) were affected by RFI.

1. We report H I absorption detections toward eight sources from 13 sources with good data. Of these eight, five absorbers are discoveries and four detections are of the lowest-radio-luminosity sources in the redshift range 0.25–0.4. The H I column densities for an assumed spin temperature of 100 K and a covering factor of 1 are in the range $\sim 2.57 \times 10^{20}$ cm⁻² to 101.92×10^{20} cm⁻², with a median value of 9.46×10^{20} cm⁻². For the H I nondetections, the median 3σ upper limit on H I column densities is 2.72×10^{20} cm⁻². Except for the sources J090410.36+024744.8, J133242.53+134253.8, and J135223.46–015648.4, all other absorption lines in our sample are narrow lines, with their FWHM < 100 km s⁻¹.
2. We find that the detection rates are primarily affected by the red mid-infrared colors, reflecting the dust- and gas-

rich nature of the host galaxies and the compactness of the radio sources. We do not find any significant dependence of the detection rates on either radio luminosity or redshift.

3. We find that the H I column densities are anticorrelated to low-frequency spectral indices ($\alpha_{150 \text{ MHz}}^{1.4 \text{ GHz}}$, $S_{\nu} \propto \nu^{-\alpha}$). Those with an inverted continuum spectrum have higher column densities.
4. For similar mid-infrared colors, the detection rate for HERGs is similar within 1σ to that of LERGs, which is consistent with our previous results for lower-redshift objects.
5. We do not detect OH absorption in any of the 23 sources with good data at OH frequencies. However, from stacking the spectra, we obtain a stringent upper limit on the OH column densities of $3.47 \times 10^{14} T_{\text{ex}}/10 \text{ K} \times 1/f_{\text{c}} \text{ cm}^{-2}$ and an $N(\text{OH})/N(\text{H I})$ ratio = 1.78×10^{-7} for sources with H I absorption. Upon stacking, we find the OH column density 3σ upper limit for associated absorbing systems is lower than the intervening ones and the $[\text{OH}]/[\text{H I}]$ upper limit for low-intermediate-redshift systems is lower than the high-redshift absorbers.
6. Large ongoing H I and OH absorption surveys (Hu et al. 2023, Aditya et al. 2024, Deka et al. 2024) with Square Kilometre Array pathfinders will be useful for probing these findings further, using larger samples.

Acknowledgments

We thank an anonymous reviewer for the useful comments and suggestions that helped to improve the paper significantly. This work has used data from the Five-hundred-meter Aperture Spherical radio Telescope (FAST). FAST is a Chinese national megascience facility, operated by the National Astronomical Observatories of the Chinese Academy of Sciences (NAOC). This work is supported in part by the National Natural Science Foundation of China (NSFC) under grant No. 11988101, 12050410259, 12373012, U1931110, and 12041302. Y.C. thanks the Center for Astronomical Mega-Science, Chinese Academy of Sciences, for the FAST distinguished young researcher fellowship (19-FAST-02). Y.C. also acknowledges the support from the Ministry of Science and Technology (MOST) of China grant No. QNJ2021061003L. Y.Z.M. acknowledges the support from the National Research Foundation of South Africa with grant Nos. 150580, 159044, CHN22111069370, and ERC23040389081. Z.Z. is supported by the Young Researcher Grant of the Institutional Center for Shared Technologies and Facilities of National Astronomical Observatories, Chinese Academy of Sciences. D.T. acknowledges financial support from the XJTLU Research Development Fund (RDF) grant with number RDF-22-02-068. H.P. acknowledges support from a UKRI Frontiers Research grant (EP/X026639/1), which was selected by the ERC.

This publication makes use of data products from the Wide-field Infrared Survey Explorer, which is a joint project of the University of California, Los Angeles, and the Jet Propulsion Laboratory/California Institute of Technology, and NEOWISE, which is a project of the Jet Propulsion Laboratory/California Institute of Technology. WISE and NEOWISE are funded by the National Aeronautics and Space Administration. Funding for the Sloan Digital Sky Survey (SDSS) has been provided by the Alfred P. Sloan Foundation, the Participating Institutions, the National Aeronautics and Space Administration, the National Science Foundation, the U.S. Department of Energy, the

Japanese Monbukagakusho, and the Max Planck Society. The SDSS website is <http://www.sdss.org/>. The SDSS is managed by the Astrophysical Research Consortium (ARC) for the Participating Institutions. The Participating Institutions are the University of Chicago, Fermilab, the Institute for Advanced Study, the Japan Participation Group, the Johns Hopkins University, Los Alamos National Laboratory, the Max-Planck-Institute for Astronomy (MPIA), the Max-Planck-Institute for Astrophysics (MPA), New Mexico State University, University of Pittsburgh, Princeton University, the United States Naval Observatory, and the University of Washington.

Facility: FAST (Nan et al. 2011).

Software: Python, Numpy (Harris et al. 2020), Matplotlib (Hunter 2007), Astropy (Astropy Collaboration et al. 2013, 2018, 2022), TOPCAT (Taylor 2005).

ORCID iDs

Yogesh Chandola  <https://orcid.org/0000-0002-3698-3294>

D. J. Saikia  <https://orcid.org/0000-0002-4464-8023>

Yin-Zhe Ma  <https://orcid.org/0000-0001-8108-0986>

Chao-Wei Tsai  <https://orcid.org/0000-0002-9390-9672>

Di Li  <https://orcid.org/0000-0003-3010-7661>

Denis Tramonte  <https://orcid.org/0000-0002-6754-1448>

References

- Aditya, J. N. H. S., & Kanekar, N. 2018a, *MNRAS*, 481, 1578
- Aditya, J. N. H. S., & Kanekar, N. 2018b, *MNRAS*, 473, 59
- Aditya, J. N. H. S., Kanekar, N., & Kurapati, S. 2016, *MNRAS*, 455, 4000
- Aditya, J. N. H. S., Yoon, H., Allison, J. R., et al. 2024, *MNRAS*, 527, 8511
- Ahumada, R., Allende Prieto, C., Almeida, A., et al. 2020, *ApJS*, 249, 3
- Allen, S. W., Dunn, R. J. H., Fabian, A. C., Taylor, G. B., & Reynolds, C. S. 2006, *MNRAS*, 372, 21
- An, T., & Baan, W. A. 2012, *ApJ*, 760, 77
- Araya, E. D., Rodríguez, C., Pihlström, Y., et al. 2010, *AJ*, 139, 17
- Astropy Collaboration, Price-Whelan, A. M., Lim, P. L., et al. 2022, *ApJ*, 935, 167
- Astropy Collaboration, Price-Whelan, A. M., Sipőcz, B. M., et al. 2018, *AJ*, 156, 123
- Astropy Collaboration, Robitaille, T. P., Tollerud, E. J., et al. 2013, *A&A*, 558, A33
- Becker, R. H., White, R. L., & Helfand, D. J. 1995, *ApJ*, 450, 559
- Best, P. N., & Heckman, T. M. 2012, *MNRAS*, 421, 1569
- Bondi, H. 1952, *MNRAS*, 112, 195
- Buttiglione, S., Capetti, A., Celotti, A., et al. 2010, *A&A*, 509, A6
- Chandola, Y., Gupta, N., & Saikia, D. J. 2013, *MNRAS*, 429, 2380
- Chandola, Y., & Saikia, D. J. 2017, *MNRAS*, 465, 997
- Chandola, Y., Saikia, D. J., & Li, D. 2020, *MNRAS*, 494, 5161
- Chandola, Y., Sirothia, S. K., & Saikia, D. J. 2011, *MNRAS*, 418, 1787
- Condon, J. J., Cotton, W. D., Greisen, E. W., et al. 1998, *AJ*, 115, 1693
- Curran, S. J. 2024, *PASA*, 41, e007
- Curran, S. J., Allison, J. R., Glowacki, M., Whiting, M. T., & Sadler, E. M. 2013, *MNRAS*, 431, 3408
- Curran, S. J., Hunstead, R. W., Johnston, H. M., et al. 2019, *MNRAS*, 484, 1182
- Curran, S. J., Whiting, M. T., Allison, J. R., et al. 2017, *MNRAS*, 467, 4514
- Curran, S. J., Whiting, M. T., Murphy, M. T., et al. 2006, *MNRAS*, 371, 431
- Curran, S. J., Whiting, M. T., Webb, J. K., & Athreya, R. 2011, *MNRAS*, 414, L26
- Curran, S. J., Whiting, M. T., Wiklind, T., et al. 2008, *MNRAS*, 391, 765
- Cutri, R. M., Wright, E. L., Conrow, T., et al. 2021, *VizieR On-line Data Catalog/II/328*
- D'Abusco, R., Massaro, F., Paggi, A., et al. 2014, *ApJS*, 215, 14
- Davies, R. L., Belli, S., Park, M., et al. 2024, *MNRAS*, 528, 4976
- de Gasperin, F., Intema, H. T., & Frail, D. A. 2018, *MNRAS*, 474, 5008
- Deka, P. P., Gupta, N., Chen, H. W., et al. 2024, *A&A*, 687, A50
- Ellison, S. L., Mendel, J. T., Patton, D. R., & Scudder, J. M. 2013, *MNRAS*, 435, 3627
- Emonts, B. H. C., Morganti, R., Struve, C., et al. 2010, *MNRAS*, 406, 987
- Gaspari, M., Ruszkowski, M., & Oh, S. P. 2013, *MNRAS*, 432, 3401
- Gehrels, N. 1986, *ApJ*, 303, 336
- Geréb, K., Maccagni, F. M., Morganti, R., & Oosterloo, T. A. 2015, *A&A*, 575, A44
- Grasha, K., Darling, J., Bolatto, A., Leroy, A. K., & Stocke, J. T. 2019, *ApJS*, 245, 3
- Gupta, N., Momjian, E., Srianand, R., et al. 2018, *ApJL*, 860, L22
- Gupta, N., Salter, C. J., Saikia, D. J., Ghosh, T., & Jeyakumar, S. 2006, *MNRAS*, 373, 972
- Hardcastle, M. J., Evans, D. A., & Croston, J. H. 2007, *MNRAS*, 376, 1849
- Harris, C. R., Millman, K. J., van der Walt, S. J., et al. 2020, *Natur*, 585, 357
- Harrison, C. M. 2017, *NatAs*, 1, 0165
- Harrison, C. M., & Ramos Almeida, C. 2024, *Galax*, 12, 17
- Heckman, T. M., & Best, P. N. 2014, *ARA&A*, 52, 589
- Helmboldt, J. F., Taylor, G. B., Tremblay, S., et al. 2007, *ApJ*, 658, 203
- Hine, R. G., & Longair, M. S. 1979, *MNRAS*, 188, 111
- Hopkins, P. F., Hernquist, L., Cox, T. J., et al. 2006, *ApJS*, 163, 1
- Hunter, J. D. 2007, *CSE*, 9, 90
- Hu, W., Wang, Y., Li, Y., et al. 2023, *A&A*, 675, A40
- Intema, H. T., Jagannathan, P., Mooley, K. P., & Frail, D. A. 2017, *A&A*, 598, A78
- Jiang, P., Tang, N.-Y., Hou, L.-G., et al. 2020, *RAA*, 20, 064
- Kanekar, N., & Briggs, F. H. 2003, *A&A*, 412, L29
- Kanekar, N., Carilli, C. L., Langston, G. I., et al. 2005, *PhRvL*, 95, 261301
- Kanekar, N., & Chengalur, J. N. 2002, *A&A*, 381, L73
- Kanekar, N., Langston, G. I., Stocke, J. T., Carilli, C. L., & Menten, K. M. 2012, *ApJL*, 746, L16
- Kormendy, J., & Ho, L. C. 2013, *ARA&A*, 51, 511
- Kunert-Bajraszewska, M., Gawrońska, M. P., Labiano, A., & Siemiginowska, A. 2010, *MNRAS*, 408, 2261
- Laing, R. A., Jenkins, C. R., Wall, J. V., & Unger, S. W. 1994, in *ASP Conf. Ser. 54, The Physics of Active Galaxies*, ed. G. V. Bicknell, M. A. Dopita, & P. J. Quinn (San Francisco, CA: ASP), 201
- Li, D., Tang, N., Nguyen, H., et al. 2018, *ApJS*, 235, 1
- Liszt, H., & Lucas, R. 1996, *A&A*, 314, 917
- Maccagni, F. M., Morganti, R., Oosterloo, T. A., Geréb, K., & Maddox, N. 2017, *A&A*, 604, A43
- Mahony, E. K., Allison, J. R., Sadler, E. M., et al. 2022, *MNRAS*, 509, 1690
- McBride, J., Heiles, C., & Elitzur, M. 2013, *ApJ*, 774, 35
- Morganti, R., Fogasy, J., Paragi, Z., Oosterloo, T., & Orienti, M. 2013, *Sci*, 341, 1082
- Morganti, R., Murthy, S., Oosterloo, T., et al. 2023, *A&A*, 678, A42
- Morganti, R., & Oosterloo, T. 2018, *A&ARv*, 26, 4
- Morganti, R., Oosterloo, T., & Tsvetanov, Z. 1998, *AJ*, 115, 915
- Morganti, R., Oosterloo, T. A., Emonts, B. H. C., van der Hulst, J. M., & Tadhunter, C. N. 2003, *ApJL*, 593, L69
- Morganti, R., Peck, A. B., Oosterloo, T. A., et al. 2009, *A&A*, 505, 559
- Mukherjee, D., Bicknell, G. V., Wagner, A. Y., Sutherland, R. S., & Silk, J. 2018a, *MNRAS*, 479, 5544
- Mukherjee, D., Wagner, A. Y., Bicknell, G. V., et al. 2018b, *MNRAS*, 476, 80
- Mulcahey, C. R., Leslie, S. K., Jackson, T. M., et al. 2022, *A&A*, 665, A144
- Murthy, S., Morganti, R., Kanekar, N., & Oosterloo, T. 2022, *A&A*, 659, A185
- Murthy, S., Morganti, R., Oosterloo, T., & Maccagni, F. M. 2021, *A&A*, 654, A94
- Murthy, S., Morganti, R., Oosterloo, T., Schulz, R., & Paragi, Z. 2024, *A&A*, 688, A84
- Nan, R., Li, D., Jin, C., et al. 2011, *IJMPD*, 20, 989
- O'Dea, C. P., & Saikia, D. J. 2021, *A&ARv*, 29, 3
- Ostorero, L., Morganti, R., Diaferio, A., et al. 2017, *ApJ*, 849, 34
- Peña-Herazo, H. A., Massaro, F., Gu, M., et al. 2021, *AJ*, 161, 196
- Pihlström, Y. M., Conway, J. E., & Vermeulen, R. C. 2003, *A&A*, 404, 871
- Saikia, D. J. 2022, *JApA*, 43, 97
- Schneider, D. P., Hall, P. B., Richards, G. T., et al. 2005, *AJ*, 130, 367
- Struve, C., & Conway, J. E. 2012, *A&A*, 546, A22
- Su, R., Gu, M., Curran, S. J., et al. 2023, *ApJL*, 956, L28
- Taylor, G. B., Vermeulen, R. C., Readhead, A. C. S., et al. 1996, *ApJS*, 107, 37
- Taylor, M. B. 2005, in *ASP Conf. Ser. 347, Astronomical Data Analysis Software and Systems XIV*, ed. P. Shopbell, M. Britton, & R. Ebert (San Francisco, CA: ASP), 29
- Tremblay, G. R., Combes, F., Oonk, J. B. R., et al. 2018, *ApJ*, 865, 13
- Vermeulen, R. C., Pihlström, Y. M., Tschager, W., et al. 2003, *A&A*, 404, 861
- Wolfe, A. M., & Burbidge, G. R. 1975, *ApJ*, 200, 548
- Wright, E. L., Eisenhardt, P. R. M., Mainzer, A. K., et al. 2010, *AJ*, 140, 1868
- Yan, T., Stocke, J. T., Darling, J., et al. 2016, *AJ*, 151, 74
- Yu, Q., Fang, T., Wang, J., & Wu, J. 2023, *ApJ*, 952, 144
- Zhang, K., Wu, J., Li, D., et al. 2019, *SCPMA*, 62, 959506
- Zheng, Z., Li, D., Sadler, E. M., Allison, J. R., & Tang, N. 2020, *MNRAS*, 499, 3085